
3DP3: 3D Scene Perception via Probabilistic Programming

Nishad Gothoskar¹Marco Cusumano-Towner¹Ben Zinberg¹Matin Ghavamizadeh¹Falk Pollok²Austin Garrett¹Joshua B. Tenenbaum¹Dan Gutfreund²Vikash K. Mansinghka¹¹MIT²MIT-IBM Watson AI Lab

{nishad,marcoct,bzinberg,mghavami,jbt,vkm}@mit.edu

{falk.pollok,austin.garrett}@ibm.com dgutfre@us.ibm.com

Abstract

We present 3DP3, a framework for inverse graphics that uses inference in a structured generative model of objects, scenes, and images. 3DP3 uses (i) voxel models to represent the 3D shape of objects, (ii) hierarchical scene graphs to decompose scenes into objects and the contacts between them, and (iii) depth image likelihoods based on real-time graphics. Given an observed RGB-D image, 3DP3’s inference algorithm infers the underlying latent 3D scene, including the object poses and a parsimonious joint parametrization of these poses, using fast bottom-up pose proposals, novel involutive MCMC updates of the scene graph structure, and, optionally, neural object detectors and pose estimators. We show that 3DP3 enables scene understanding that is aware of 3D shape, occlusion, and contact structure. Our results demonstrate that 3DP3 is more accurate at 6DoF object pose estimation from real images than deep learning baselines and shows better generalization to challenging scenes with novel viewpoints, contact, and partial observability.

1 Introduction

A striking feature of human visual intelligence is our ability to learn representations of novel objects from a limited amount of data and then robustly perceive 3D scenes containing those objects. We can immediately generalize across large variations in viewpoint, occlusion, lighting, and clutter. How might we develop computational vision systems that can do the same?

This paper presents a generative model for 3D scene perception, called 3DP3. Object shapes are learned via probabilistic inference in a voxel occupancy model that coarsely captures 3D shape and uncertainty due to self-occlusion (Section 4). Scenes are modeled via hierarchical 3D scene graphs that can explain planar contacts between objects without forcing scenes to fit rigid structural assumptions (Section 3). Images are modeled by real-time graphics and robust likelihoods on point clouds. We cast 3D scene understanding as approximate probabilistic inference in this generative model. We develop a novel inference algorithm that combines data-driven Metropolis-Hastings kernels over object poses, involutive MCMC kernels over scene graph structure, pseudo-marginal integration over uncertain object shape, and existing deep learning object detectors and pose estimators (Section 5). This architecture leverages inference in the generative model to provide common sense constraints that fix errors made by bottom-up neural detectors. Our experiments show that 3DP3 is more accurate and robust than deep learning baselines at 6DoF pose estimation for challenging synthetic and real-world scenes (Section 6). Our model and inference algorithm are implemented in the Gen [13] probabilistic programming system.

2 Related Work

Analysis-by-synthesis approaches to computer vision A long line of work has interpreted computer vision as the inverse problem to computer graphics [25, 45, 30, 26]. This ‘analysis-by-synthesis’ approach has been used for various tasks including character recognition, CAPTCHA-breaking, lane detection, object pose estimation, and human pose estimation [46, 41, 31, 34, 21, 35]. To our knowledge, our work is the first to use an analysis-by-synthesis approach to infer a hierarchical 3D object-based representation of real multi-object scenes while exploiting inductive biases about the contacts between objects.

Hierarchical latent 3D scene representations We use a scene graph representation [47] that is closely related to hierarchical scene graph representations in computer graphics [11]. Unlike in graphics, we address the *inverse problem* of inferring hierarchical scene graphs from observed image data. Inferring hierarchical 3D scene graphs from RGB or depth images in a probabilistic framework is relatively unexplored. One concurrent¹ and independent work, Generative Scene Graph Networks (GSGN [15]), proposes a variational autoencoder architecture for decomposing images into objects and parts using a tree-structured latent scene graph that is similar to our scene graph representation. However, GSGN learns RGB appearance models of objects and their parts, uses an inference network instead of a hybrid of data-driven and model-based inference, was not evaluated on real images or scenes, and uses more restricted scene graphs that cannot represent objects with independent 6DoF pose. GSGN builds on an earlier deep generative model [19] that generates multi-object scenes but does not model dependencies between object poses and was not quantitatively evaluated on real 3D scenes. Incorporating a learned inference network for jointly proposing scene graphs into our framework is an interesting area for future work. The term ‘scene graph’ has also been used in computer vision to refer to various less related graph representations of scenes [3, 10, 36].

Probabilistic programming for computer vision Prior work has used probabilistic programs to represent generative models of images and implemented inference in these models using probabilistic programming systems [31, 28]. Unlike these prior works, which relied on manually specified and/or semi-parametric shape models, 3DP3 learns object shapes non-parametrically. 3DP3 also models occlusion of one 3D object by another; uses a novel hierarchical scene graph prior that allows for dependencies between object poses in the prior; uses a novel involutive MCMC [12] kernel for inferring scene graph structure; and uses a novel pseudo-marginal approach for handling uncertainty about object shape during inference. We also present a proof of concept that our system can infer the presence and pose of fully occluded objects.

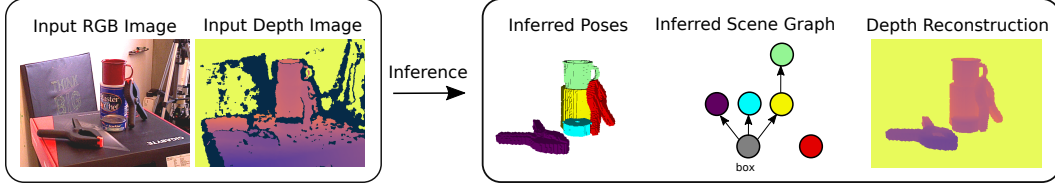
6DoF object pose estimation We use 6DoF estimation of object pose from RGBD images as an example application. Registration of point clouds [6] can be used to estimate the 6DoF pose of objects with known 3D geometry from depth images. Many recent 6DoF object pose estimators use deep learning [43, 40] and many also take depth images [42, 39]. Some pose estimation methods model scene structure, contact relationships, stability, or other semantic information [24, 10, 27, 18, 5], and some use probabilistic inference [17, 9, 22, 16]. To our knowledge, we present the first 6DoF pose estimator that uses Bayesian inference about the structure of hierarchical 3D scene graphs.

Learning models of novel 3D objects Classic algorithms for structure-from-motion infer a 3D model of a scene from multiple images [38, 1]. Our approach for learning the shape of novel 3D objects produces coarse-grained probabilistic voxel models of objects that can represent uncertainty about the occupancy of self-occluded volumes. Integrating other representations of object shape and object appearance [33] with our scene graph representation is a promising area of future work.

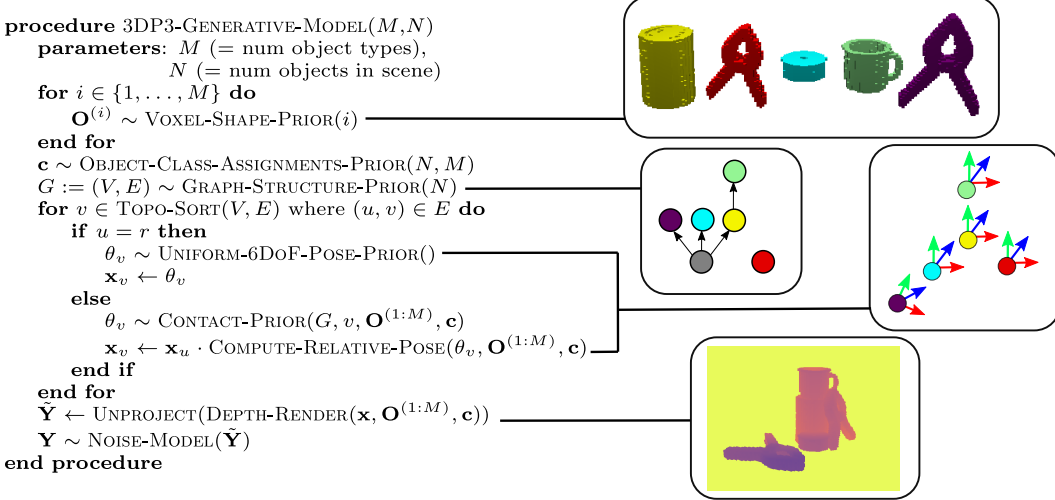
3 3DP3 generative modeling framework

The core of 3DP3 is a generative modeling framework that represents a scene in terms of discrete objects, the 3D shape of each object, and a hierarchical structure called a scene graph that relates the poses (position and orientation) of the objects. This section describes 3DP3’s object shape and scene graph latent representations, a family of prior distributions on these latent representations, and an observation model for image-based observations of scenes. Figure 1 shows the combined generative model written as a probabilistic program.

¹An early version of our work [47] is concurrent with an early version of GSGN [14]



(a) Inferring a hierarchical 3D scene graph from an RGB-D image with 3DP3. Our model knows that objects often lay flat on other objects, which allows for the depth pixels of one object to inform the pose of other objects. Our algorithm also infers when this knowledge is relevant (e.g. the clamp on the left, represented by the purple node, is laying flat on the box), and when it is not (e.g. the clamp on the right, represented by the red node, is not laying flat on any other object).



(b) 3DP3 uses a structured generative model of 3D scenes, represented as a probabilistic program. The model uses a prior over object shapes that can be learned from data, a prior over scene structure that is a probability distribution on graphs, a traversal of the scene graph starting at the world node r to compute object poses, and a robust likelihood model for depth images. In the graph at right, the world node r (not shown) is the parent of the grey node (box) and the red node (right clamp) because those objects are not laying flat on other objects.

Figure 1: (a) A scene graph inference task and (b) the 3DP3 generative model.

3.1 Objects

The most basic element of our generative modeling framework are rigid objects. The first stage in our generative model prior encodes uncertainty about the 3D shape of M types of rigid objects that may or may not be encountered in any given scene.

Voxel 3D object shapes We model the coarse 3D shape of rigid objects using a voxel grid with dimensions $h, w, l \in \mathbb{N}$ and cells indexed by $(i, j, \ell) \in [h] \times [w] \times [l]$. Each cell has dimension $s \times s \times s$ for resolution $s \in \mathbb{R}^+$, so that the entire voxel grid represents the cuboid $[0, h \cdot s] \times [0, w \cdot s] \times [0, l \cdot s]$. All objects are assumed to fit within the cuboid. An object’s *shape* is defined by a binary assignment $\mathbf{O} \in \{0, 1\}^{h \times w \times l}$ of occupancy states to each cell in the voxel grid, where $O_{ij\ell} = 1$ indicates that cell (i, j, ℓ) is occupied and $O_{ij\ell} = 0$ indicates it is free. Each object also has a finite set of *contact planes* through which the object may be in flush contact with the contact planes of other objects in physically stable scenes. For example, in Figure 2, the table has a contact plane for its top surface, the yellow sugar box has six contact planes, one for each of its six faces, and the bottom contact plane of the sugar box is in flush contact with the top contact plane of the table. The pose of a contact plane relative to its object is a function of the object shape \mathbf{O} . To simplify notation, we denote the set of contact planes for any object by F .

Prior distributions on 3D object shape We assume there are M distinct object types, and each object type $m \in \{1, \dots, M\}$ has an a-priori unknown shape, denoted $\mathbf{O}^{(m)}$. Let $\mathbf{O}^{(1:M)} :=$

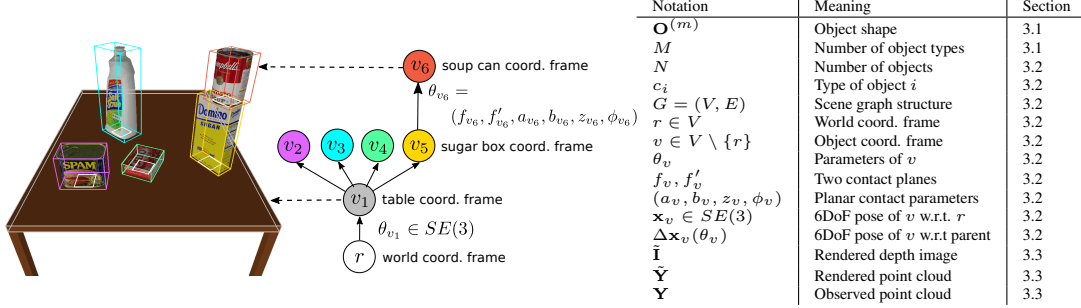


Figure 2: Our hierarchical scene graphs encode a tree of coordinate frames representing entities in a scene and their geometric relationships (e.g. flush contact between faces of two objects).

$(\mathbf{O}^{(1)}, \dots, \mathbf{O}^{(M)})$. The prior distribution on the shape of each object type m is denoted $p(\mathbf{O}^{(m)})$. Although our inference algorithm (Section 5) only requires the ability to sample jointly from $p(\mathbf{O}^{(1:M)})$, we assume shapes of object types are independent in the prior ($p(\mathbf{O}^{(1:M)}) = \prod_{m=1}^M p(\mathbf{O}^{(m)})$). Section 4 shows how to learn a specific shape prior $p(\mathbf{O}^{(m)})$ for an object type from depth images.

3.2 Scenes

Given a collection of M known object types and their shapes, our model generates scenes with N objects by randomly selecting an object type for each object and then sampling a 6DoF object pose for each object. Instead of assuming that object poses are independent, our model encodes an inductive bias about the regularities in real-world scenes: objects are often resting in flush contact with other objects (e.g. see Figure 2). We jointly sample *dependent* object poses using a flexible hierarchical scene graph, while maintaining uncertainty over the structure of the graph.

Hierarchical scene graphs We model the geometric state of a scene as a *scene graph* \mathcal{G} (Figure 2), which is a tuple $\mathcal{G} = (G, \theta)$ where $G = (V, E)$ is a directed rooted tree and θ are parameters. The vertices $V := \{r, v_1, \dots, v_N\}$ represent $N + 1$ 3D coordinate frames, with r representing the world coordinate frame. An edge $(u, v) \in E$ indicates that coordinate frame v is parametrized relative to frame u , with parameters θ_v . The 6DoF pose of frame v relative to frame u with pose $\mathbf{x}_u \in SE(3)$ is given by a function $\Delta \mathbf{x}_v$, where $\Delta \mathbf{x}_v(\theta_v) \in SE(3)$ and $\mathbf{x}_v := \mathbf{x}_u \cdot \Delta \mathbf{x}_v(\theta_v)$. Here, \cdot is the $SE(3)$ group operation, and the world coordinate frame is defined as the identity element ($\mathbf{x}_r := I$).

Modeling flush contact between rigid objects While the vertices of scene graphs \mathcal{G} can represent arbitrary coordinate frames in a scene (e.g. the coordinate frames of articulated joints, object poses), in the remainder of this paper we assume that each vertex $v \in V \setminus \{r\}$ corresponds to the pose of a rigid object. We index objects by $1, \dots, N$, with corresponding vertices v_1, \dots, v_N . We assume that each object i has an object type $c_i \in \{1, \dots, M\}$. For vertices v that are children of the root vertex r , $\theta_v \in SE(3)$ defines the absolute 6DoF pose of the corresponding object ($\Delta \mathbf{x}_v(\theta_v) = \theta_v$). For vertices v that are children of a non-root vertex u , the parameters take the form $\theta_v = (f_v, f'_v, a_v, b_v, z_v, \phi_v)$ and represent a contact relationship between the two objects: f_v and f'_v indicate which contact planes of the parent and child objects, respectively, are in contact. $(a_v, b_v) \in \mathbb{R}^2$ is the in-plane offset of the origin of plane f_v of object v from the origin of plane f'_v of object u . $z_v \in \mathbb{R}$ is the perpendicular distance of the origin of plane f_v of object v from plane f'_v of object u . $\phi_v \in S^2 \times S^1$ represents the deviation of the normal vectors of the two contact planes from anti-parallel (in S^2) and a relative in-plane rotation of the two contact planes (in S^1). The relative pose $\Delta \mathbf{x}_v(\theta_v)$ of v with respect to u is the composition (in $SE(3)$) of three relative poses: (i) v with respect to its plane f_v , (ii) v 's plane f_v with respect to u 's plane f'_v , and (iii) u 's plane f'_v with respect to u . The 6DoF poses of all objects (\mathbf{x}_v for $v \in V \setminus \{r\}$) are computed by traversing the scene graph while taking products of relative poses along paths from the root r .

Prior distributions on scene graphs We now describe our prior on scene graphs, given object models $\mathbf{O}^{(1:M)}$. We assume the number of objects N in the scene is known (see the supplement for a generalization to unknown N). We first sample the types $c_i \in \{1, \dots, M\}$ of all objects from an

exchangeable distribution $p(\mathbf{c})$ where $\mathbf{c} := (c_1, \dots, c_N)$. This includes as a special case distributions where all types are represented at most once among the objects ($\sum_{i=1}^N \mathbf{1}[c_i = c] \leq 1$), which is the case in our experiments. Next, we sample the scene graph structure G from $p(G)$. We experiment with two priors $p(G)$: (i) a uniform distribution on the set of $(N + 1)^{N-1}$ directed trees that are rooted at a vertex r , and (ii) $\delta_{G_0}(G)$, where G_0 is a graph on $N + 1$ vertices where $(r, v) \in E$ for all $v \in V \setminus \{r\}$ so that each object vertex has an independent 6DoF pose. For objects whose parent is r (the world coordinate frame), we sample the pose $\theta_v \sim p_{\text{unif}}$, which samples the translation component uniformly from a cuboid scene extent, and the orientation uniformly over $SO(3)$. For objects whose parent is another object u , we sample the choice of contact planes $(f_v, f'_v) \in F \times F$ uniformly, $(a_v, b_v) \sim \text{Uniform}([-50\text{cm}, 50\text{cm}]^2)$, $z_v \sim \text{N}(0, 1\text{cm})$, the S^2 component of ϕ_v from a von Mises–Fisher (vMF) distribution concentrated ($\kappa = 250$) on anti-parallel plane normals, and the S^1 component from $\text{Uniform}(S^1)$. We denote this distribution $p_{\text{cont}}(\theta_v)$. Note that the parameters of p_{cont} were not tuned or tailored in any detailed way—they were chosen heuristically based on the rough dimensions of table-top objects. The resulting prior over all of the latent variables is:

$$p(\mathbf{O}^{(1:M)}, \mathbf{c}, G, \boldsymbol{\theta}) = \left(\prod_{m=1}^M p(\mathbf{O}^{(m)}) \right) \frac{1}{(N + 1)^{N-1}} p(\mathbf{c}) \prod_{\substack{v \in V: \\ (r, v) \in E}} p_{\text{unif}}(\theta_v) \prod_{\substack{(u, v) \in E: \\ u \neq r}} p_{\text{cont}}(\theta_v) \quad (1)$$

3.3 Images

Our generative model uses an observation model that generate synthetic image data given object shapes $\mathbf{O}^{(1:M)}$ and a scene graph \mathcal{G} containing N objects. We now describe the observation model for depth images that is used in our main experiments (Section 6).

Likelihood model for depth images We first convert an observed depth image into a point cloud \mathbf{Y} . To model a point cloud $\mathbf{Y} \in \mathbb{R}^{K \times 3}$ with K points denoted $\mathbf{y}_i \in \mathbb{R}^3$, we use a likelihood model based on rendering a synthetic depth image of the scene graph. Specifically, given the object models $\mathbf{O}^{(m)}$ for each $m \in \{1, \dots, M\}$, the object types \mathbf{c} , the scene graph \mathcal{G} , and the camera intrinsic and extrinsic parameters relative to the world frame, we (i) compute meshes from each $\mathbf{O}^{(m)}$, (ii) compute the 6DoF poses (\mathbf{x}_v) of objects with respect to the world frame by traversing the scene graph \mathcal{G} , and (iii) render a depth image $\tilde{\mathbf{I}}$ of \mathcal{G} using an OpenGL depth buffer, and (iv) unproject the rendered depth image to obtain a point cloud $\tilde{\mathbf{Y}}$ with \tilde{K} points (\tilde{K} is the number of pixels in the depth image). We then generate an observed point cloud $\mathbf{Y} \in \mathbb{R}^{K \times 3}$ by drawing each point from a mixture:

$$p(\mathbf{Y} | \mathbf{O}^{(1:M)}, \mathbf{c}, G, \boldsymbol{\theta}) := \prod_{i=1}^K \left(C \cdot \frac{1}{B} + \frac{1 - C}{\tilde{K}} \sum_{j=1}^{\tilde{K}} \frac{\mathbf{1}[\|\mathbf{y}_i - \tilde{\mathbf{y}}_j\|_2 \leq r]}{\frac{4}{3}\pi r^3} \right) \quad (2)$$

for some $0 < C < 1$ and some $r > 0$. The components of this mixture are uniform distributions over the balls of radius r centered at each point in $\tilde{\mathbf{Y}}$ (with weights $(1 - C)/\tilde{K}$) and a uniform distribution over the scene bounding volume B (weight C).²

4 Learning object shape models

3DP3 does not require hard-coded shape models. Instead, it uses probabilistic inference to learn non-parametric models of 3D object shape $p(\mathbf{O}^{(m)})$ that account for uncertainty due to self-occlusion. We focus on the restricted setting of learning from scenes containing a single isolated object ($N = 1$) of known type (c_1). Our approach works best for views that lead to minimal uncertainty about the exterior shape of the object; more general, flexible treatments of shape learning and shape uncertainty are beyond the scope of this paper.

First, we group the depth images by the object type (c_1), so that we have M independent learning problems. Let $\mathbf{I}_{1:T} := (\mathbf{I}_1, \dots, \mathbf{I}_T)$ denote the depth observations for one object type, with object shape denoted \mathbf{O} . The learning algorithm uses Bayesian inference in another generative model p' . The posterior $p'(\mathbf{O} | \mathbf{I}_{1:T})$ produced by this algorithm becomes the prior $p(\mathbf{O})$ used in Section 3.1.

²By using a distribution that is uniform over a small, spherical region rather than a Gaussian distribution, we avoid (via k -d trees) computing pairwise distances between all points in \mathbf{Y} and $\tilde{\mathbf{Y}}$, resulting in $\approx 10\times$ speedup.

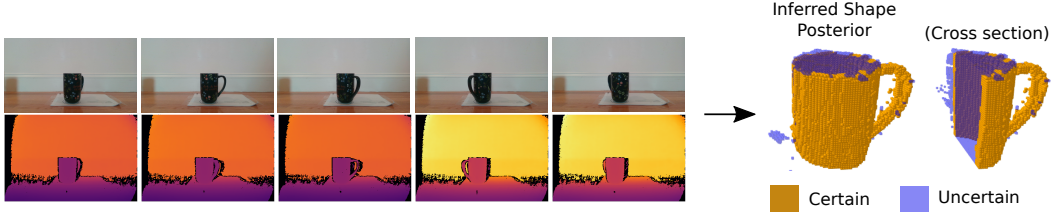


Figure 3: Learning a voxel-based shape models $p(\mathbf{O}^{(m)})$ for a novel object from a set of 5 depth images. Our shape priors capture uncertainty about voxel occupancy due to self-occlusion (right).

We start with a uninformed prior distribution $p'(\mathbf{O}) := \prod_{i=1}^h \prod_{j=1}^w \prod_{\ell=1}^l p_{\text{occ}}^{O_{ij\ell}} (1 - p_{\text{occ}})^{(1-O_{ij\ell})}$ on the 3D shape of an object type, for a per-voxel occupancy probability p_{occ} (in our experiments, 0.5). We learn about the object’s shape by observing a sequence of depth images $\mathbf{I}_{1:T}$ that contain views of the object, which is assumed to be static relative to other contents of the scene, which we call the ‘map’ \mathbf{M} . (In our experiments the map contains the novel object, a floor, a ceiling, and four walls of a rectangular room). We posit the following joint distribution over object shape (\mathbf{O}) and the observed depth images, conditioned on the map (\mathbf{M}) and the poses of the camera relative to the map over time ($\mathbf{x}_1, \dots, \mathbf{x}_T \in SE(3)$): $p'(\mathbf{O}, \mathbf{I}_{1:T} | \mathbf{M}, \mathbf{x}_{1:T}) := p'(\mathbf{O}) \prod_{t=1}^T p'(\mathbf{I}_t | \mathbf{O}, \mathbf{M}, \mathbf{x}_t)$.

The likelihood p' is a depth image likelihood on a latent 3D voxel occupancy grid (see supplement for details). For this model, we can compute $p'(\mathbf{O} | \mathbf{M}, \mathbf{x}_{1:T}, \mathbf{I}_{1:T}) = \prod_{ij\ell} p'(O_{ij\ell} | \mathbf{M}, \mathbf{x}_{1:T}, \mathbf{I}_{1:T})$ exactly using ray marching to decide if a voxel cell is occupied, unoccupied, or unobserved (due to being occluded by another occupied cell), and the resulting distribution on \mathbf{O} can be compactly represented as an array of probabilities ($\in [0, 1]^{h \times w \times l}$). However, in real-world scenarios the map \mathbf{M} and the camera poses $\mathbf{x}_{1:T}$ are not known with certainty. To handle this, our algorithm takes as input uncertain beliefs about \mathbf{M} and $\mathbf{x}_{1:T}$ ($q_{\text{SLAM}}(\mathbf{M}, \mathbf{x}_{1:T}) \approx p'(\mathbf{M}, \mathbf{x}_{1:T} | \mathbf{I}_{1:T})$) that are produced by a separate probabilistic SLAM (simultaneous localization and mapping) module, and take the form of a weighted collection of K particles ($\mathbf{M}^{(k)}, \mathbf{x}_{1:T}^{(k)}$): $q_{\text{SLAM}}(\mathbf{M}, \mathbf{x}_{1:T}) = \sum_{k=1}^K w_k \delta_{\mathbf{M}^{(k)}}(\mathbf{M}) \delta_{\mathbf{x}_{1:T}^{(k)}}(\mathbf{x}_{1:T})$. Various approaches to probabilistic SLAM can be used; we implemented it using sequential Monte Carlo (SMC) in Gen (more detail in supplement). From the beliefs $q_{\text{SLAM}}(\mathbf{M}, \mathbf{x}_{1:T})$ produced by SLAM, we approximate the object shape posterior via:

$$\hat{p}'(\mathbf{O} | \mathbf{I}_{1:T}) := \iint p'(\mathbf{O} | \mathbf{M}, \mathbf{x}_{1:T}, \mathbf{I}_{1:T}) q_{\text{SLAM}}(\mathbf{M}, \mathbf{x}_{1:T}) d\mathbf{M} d\mathbf{x}_{1:T} = \sum_{k=1}^K w_k p'(\mathbf{O} | \mathbf{M}^{(k)}, \mathbf{x}_{1:T}^{(k)}, \mathbf{I}_{1:T})$$

Note that while $p'(\mathbf{O} | \mathbf{M}^{(k)}, \mathbf{x}_{1:T}^{(k)}, \mathbf{I}_{1:T})$ for each k can be compactly represented, the mixture distribution $\hat{p}'(\mathbf{O} | \mathbf{I}_{1:T})$ lacks the conditional independencies that make this possible. To produce a more compact representation of beliefs about the object’s shape, we fit a variational approximation $q_{\varphi}(\mathbf{O})$ that assumes independence among voxels ($q_{\varphi}(\mathbf{O}) := \prod_{i \in [h]} \prod_{j \in [w]} \prod_{\ell \in [l]} \varphi_{ij\ell}^{O_{ij\ell}} \cdot (1 - \varphi_{ij\ell})^{(1-O_{ij\ell})}$) to $\hat{p}'(\mathbf{O} | \mathbf{I}_{1:T})$ using $\varphi^* := \arg \min_{\varphi} \text{KL}(\hat{p}'(\mathbf{O} | \mathbf{I}_{1:T}) || q_{\varphi}(\mathbf{O}))$ (see supplement for details). This choice of variational family is sufficient for representing uncertainty about the occupancy of voxels in the *interior* of an object shape. Note that our shape-learning experiments did not result in significant uncertainty about the *exterior* shape of objects³, and in the presence of such uncertainty, a less severe variational approximation may be needed for robust inference of scene graphs from depth images. Fig. 3 shows input depth images ($\mathbf{I}_{1:T}$) and resulting shape prior learned from $T = 5$ observations. After learning these shape distributions $q_{\varphi}(\mathbf{O}) \approx \hat{p}'(\mathbf{O} | \mathbf{I}_{1:T})$ for each distinct object type, we use them as the shape priors $p(\mathbf{O}_i)$ within the generative model of Section 3. The supplement includes the results of a quantitative evaluation of the accuracy of shape learning.

³The lack of significant exterior shape uncertainty in shape-learning experiments allowed us to implement an optimization: Instead of the relative poses of an object’s contact planes depending on \mathbf{O} as described in Section 3, we assign each object type a set of six contact planes derived from the faces of the smallest axis-aligned bounding cuboid that completely contains all occupied voxels in one sample \mathbf{O} from the learned prior $p(\mathbf{O}) := q_{\varphi}(\mathbf{O})$.

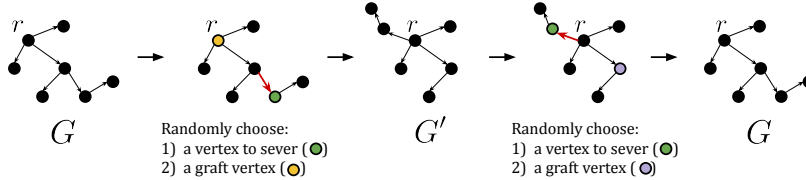


Figure 4: A reversible transition between scene graph structure G and scene graph structure G' .

5 Building blocks for approximate inference algorithms

This section first describes a set of building blocks for approximate inference algorithms that are based on the generative model of Section 3. We then describe how to combine these components into a scene graph inference algorithm that we evaluate in Section 6.

Trained object detectors It is possible to infer the types of objects in the scene (\mathbf{c}) via Bayesian inference in the generative model (see supplement for an example that infers \mathbf{c} as well as N in a scene with a fully occluded object, via Bayesian inference). However, for scenes where objects are not fully or nearly-fully occluded, and where object types have dissimilar appearance, it is possible to train fast object detectors that produce an accurate point estimate of \mathbf{c} given an RGB image.

Trained pose estimators In scenes without full or nearly-full occlusion, it is also possible to employ trained pose estimation methods [42] to give independent estimates of the 6DoF pose of each object instance in the image. However, inferring pose is more challenging than inferring \mathbf{c} , and occlusion, self-occlusion, and symmetries can introduce significant pose uncertainty. Therefore, we only use trained pose estimators (e.g. [42]) to (optionally) *initialize* the poses of objects before Bayesian inference in the generative model, using the building blocks below.

Data-driven Metropolis-Hastings kernels on object pose We employ Metropolis-Hastings (MH) kernels, parametrized by choice of object $i \in \{1, \dots, N\}$, that take as input a scene graph \mathcal{G} , propose new values (θ'_{v_i}) for the scene graph parameters of object i , construct a new proposed scene graph \mathcal{G}' , and then accept or reject the move from \mathcal{G} to \mathcal{G}' based on the MH rule. For objects v whose parent is the world frame ($(r, v) \in E$), we use a data-driven proposal distribution centered on an estimate $(\hat{\mathbf{x}}_v)$ of the 6DoF object pose obtained with ICP (a spherical normal distribution concentrated around the estimated position, and a vMF distribution concentrated around the estimated orientation). We also use kernels with random-walk proposals centered on the current pose. For objects whose parent is another object ($(u, v) \in E$ for $u \neq r$), we use a random-walk proposal on parameters $(a_{v_i}, b_{v_i}, z_{v_i})$. Note that when the pose of an object is changed in the proposed graph \mathcal{G}' , the pose of any descendant objects is also changed.⁴ Each of these MH kernels is invariant with respect to $p(G, \theta | \mathbf{c}, \mathbf{Y})$.

Involutive MCMC kernel on scene graph structure To infer the scene graph structure G , we employ a family of involutive MCMC kernels [12] that propose a new graph structure G' while keeping the poses (\mathbf{x}_v) of all objects fixed. The kernel takes a graph structure G and proposes a new graph structure G' (Figure 4) by: (i) randomly sampling a node $v \in V \setminus \{r\}$ to ‘sever’ from the tree, (ii) randomly choosing a node $u \in V \setminus \{v\}$ that is not a descendant of the severed node on which to graft v , (iii) forming a new directed graph G' over vertices V by grafting v to u ; by Lemma O.7.1 the resulting graph G' is also a tree. Note that there is an involution g on the set of all pairs (G, v, u) satisfying the above constraints. That is, if $(G', v', u') = g(G, v, u)$ then $(G, v, u) = g(G', v', u')$. (This implies, for example, that u' is the parent of v in G .) Note that this set of transitions is capable of changing the parent vertex of an object to a different parent object, changing the parent vertex of an object from the root (world frame) to any other object, or changing the parent vertex from another object to the root, depending on the random choice of v and u . We compute new values for parameters (θ_v) for the severed node v and possibly other vertices such that the poses of all vertices are unchanged. See supplement for the full kernel and a proof that it is invariant w.r.t. $p(G, \theta | \mathbf{c}, \mathbf{Y})$.

⁴It is possible to construct an involutive MCMC kernel that does not change the poses of descendant objects.



Figure 5: Qualitative comparison between DenseFusion’s pose estimates (top row) and estimates from 3DP3-based algorithm that is initialized with DenseFusion (bottom row) for YCB-Video frames where DenseFusion gives incorrect results. 3DP3’s depth-rendering likelihood and scene graph prior can correct large errors made by DenseFusion.

Approximately Rao–Blackwellizing object shape via pseudo-marginal MCMC The acceptance probability expressions for our involutive MCMC and MH kernels targeting $p(G, \theta | \mathbf{c}, \mathbf{Y})$ include factors of the form $p(\mathbf{Y} | \mathbf{c}, G, \theta)$, which is an intractable sum over the latent object models: $p(\mathbf{Y} | \mathbf{c}, G, \theta) = \sum_{\mathbf{O}^{(1:M)}} p(\mathbf{O}^{(1:M)}) p(\mathbf{Y} | \mathbf{O}^{(1:M)}, \mathbf{c}, G, \theta)$. To overcome this challenge, we employ a pseudo-marginal MCMC approach [2] that uses unbiased estimates of $p(\mathbf{Y} | \mathbf{c}, G, \theta)$ obtained via likelihood weighting (that is, sampling several times from $p(\mathbf{O}^{(1:M)})$ and averaging the resulting $p(\mathbf{Y} | \mathbf{O}^{(1:M)}, \mathbf{c}, G, \theta)$). The resulting MCMC kernels are invariant with respect to an extended target distribution of which $p(G, \theta | \mathbf{c}, \mathbf{Y})$ is a marginal (see supplement for details). We implemented an optimization where we sampled 5 values for $\mathbf{O}^{(1:M)}$ and used these samples within every estimate of $p(\mathbf{Y} | \mathbf{c}, G, \theta)$ instead of sampling new values for each estimate. Because our learned shape priors did not have significant exterior shape uncertainty, this optimization did not negatively impact the results.

Scene graph inference and implementation The end-to-end scene graph inference algorithm has three stages. First, we obtain \mathbf{c} from either an object detector or because it is given as part of the task (this is the case in our experiments; see Section 6 for details). Second, we obtain initial estimates $\hat{\mathbf{x}}_v$ of 6DoF object poses \mathbf{x}_v for all object vertices v via maximum-a-posteriori (MAP) inference in a restricted variant of the generative model with graph structure G fixed to G_0 (so there are no edges between object vertices). This MAP inference stage uses the data-driven Metropolis-Hastings kernels on poses, and (optionally) trained pose estimators (see Section 6 for the details, which differ between experiments). Third, we use the estimated poses to initialize an MCMC algorithm targeting $p(G, \theta | \mathbf{c}, \mathbf{Y})$ with state $G \leftarrow G_0$ and $\theta_v \leftarrow \hat{\mathbf{x}}_v$ for each $v \in V \setminus \{r\}$. The Markov chain is a cycle of the involutive MCMC kernel described above with a mixture of the Metropolis-Hastings kernels described above, uniformly mixed over objects. We wrote the probabilistic program of Figure 1 in Gen’s built-in modeling language. We implemented the data-driven and involutive MCMC kernels, and pseudo-marginal likelihood, and integrated all components together, using Gen’s programmable inference support. Our code is available at <https://github.com/probcomp/ThreeDP3>.

6 Experiments

We evaluate our scene graph inference algorithm on the YCB-Video [7] dataset consisting of real RGB-D images and YCB-Challenging, our own synthetic dataset of scenes containing novel viewpoints, occlusions, and contact structure. We use the evaluation protocol of the Benchmark for 6DoF Object Pose Estimation (BOP) Challenge [23], in which an RGB-D image and the number of objects in the scene and their types are given, and the task is to estimate the 6DoF pose of each object.

6.1 Pose estimation from real RGB-D images

YCB-Video is a standard robotics dataset for training and evaluating 3D perception systems [7]. We first learn shape priors (Section 4) from just 5 synthetic images for each object type. We use DenseFusion [42], a neural 6DoF pose estimator, for pose initialization in the MAP phase of our inference algorithm. To measure pose estimation accuracy, we use the average closest point distance (ADD-S [43, 42]) which estimates the average closest point distance between points on the object model placed at the predicted pose and points on the model placed at the ground-truth pose. Table 1

Object Type	# of Scenes	0.5cm Threshold			1.0cm Threshold			2.0cm Threshold		
		Accuracy			Accuracy			Accuracy		
		3DP3	3DP3*	DF	3DP3	3DP3*	DF	3DP3	3DP3*	DF
002_master_chef_can	1006	0.74	0.79	0.84	0.99	1.00	1.00	1.00	1.00	
003_cracker_box	868	0.90	0.83	0.79	0.99	0.98	0.97	0.99	0.99	
004_sugar_box	1182	1.00	0.99	0.98	1.00	1.00	1.00	1.00	1.00	
005_tomato_soup_can	1440	0.95	0.93	0.93	0.97	0.97	0.97	0.97	0.97	
006_mustard_bottle	357	0.99	0.98	0.94	0.99	0.99	0.98	1.00	1.00	
007_tuna_fish_can	1148	0.81	0.80	0.91	1.00	1.00	0.99	1.00	1.00	
008_pudding_box	214	1.00	0.97	0.70	1.00	1.00	1.00	1.00	1.00	
009_gelatin_box	214	1.00	1.00	1.00	1.00	1.00	1.00	1.00	1.00	
010_potted_meat_can	766	0.80	0.78	0.79	0.89	0.88	0.87	0.93	0.93	
011_banana	379	0.98	0.96	0.82	1.00	1.00	0.97	1.00	1.00	
019_pitcher_base	570	1.00	0.99	0.99	1.00	1.00	1.00	1.00	1.00	
021_bleach_cleanser	1029	0.94	0.88	0.80	1.00	1.00	0.99	1.00	1.00	
024_bowl	406	0.93	0.87	0.50	0.96	0.96	0.56	0.96	0.96	
025_mug	636	0.89	0.89	0.92	0.98	0.98	0.99	1.00	1.00	
035_power_drill	1057	0.98	0.96	0.88	0.99	0.99	0.98	0.99	0.99	
036_wood_block	242	0.36	0.33	0.07	0.96	0.93	0.88	1.00	1.00	
037_scissors	181	0.75	0.69	0.20	0.87	0.84	0.70	0.99	0.99	
040_large_marker	648	1.00	1.00	0.99	1.00	1.00	1.00	1.00	1.00	
051_large_clamp	712	0.68	0.64	0.25	0.71	0.70	0.33	0.79	0.79	
052_extra_large_clamp	682	0.33	0.27	0.12	0.38	0.34	0.17	0.69	0.70	
061_foam_brick	288	0.26	0.24	0.01	1.00	1.00	0.99	1.00	1.00	

Table 1: Accuracy results on the real YCB-Video test set, for accuracy thresholds 0.5cm, 1.0cm, and 2.0cm, and per object type. 3DP3 is our full scene graph inference algorithm and 3DP3* is an ablation that does not infer contact relationships. ‘# of Scenes’ = The number of test images in which that object appears, out of the total 2,949 images. ‘DF’ = DenseFusion [42], a deep learning baseline.

shows the quantitative results. For almost all objects, our algorithm (3DP3) is more accurate than an ablation (3DP3*) that fixes the structure so that there are no contact relationships, and the ablation is more accurate than DenseFusion. This suggests that both the rendering-based likelihood and inference of structure contribute to 3DP3’s more accurate 6DoF pose estimation. Figure 5 shows examples of corrections that 3DP3 makes to DenseFusion’s estimates.

6.2 Generalization to challenging scenes

Next, we evaluated our algorithm’s performance on challenging scenes containing novel viewpoints, occlusions, and contact structure. Our synthetic YCB-Challenging dataset consists of 2000 RGB-D images containing objects from the YCB object set [7] in the following 4 categories of challenging scenes: (i) *Single object*: Single object in contact with table, (ii) *Stacked*: Stack of two objects on a table, (iii) *Partial view*: Single object not fully in field-of-view, (iv) *Partially Occluded*: One object partially occluded by another. For this experiment, the MAP stage of our algorithm uses an alternative initialization (see supplement) that does not use DenseFusion. We evaluate 3DP3 and the 3DP3* ablation alongside DenseFusion [42] and another state-of-the-art baseline, Robust6D [39]. For most scenes and objects, our approach significantly outperforms the baselines (Table 2). In Table 3, we assess 3DP3’s robustness by inspecting the error distribution at the 1st, 2nd, and 3rd quartile for each scene type and object type. At Q3, 3DP3 consistently outperforms the baselines and we find that the drop in performance from Q1 and Q3 is less for 3DP3 than the baselines.

7 Discussion

This paper presented 3DP3, a framework for generative modeling, learning, and inference with structured scenes and image data; and showed that it improves the accuracy of 6DoF object pose estimation in cluttered scenes. We used probabilistic programs to conceive of our generative model and represent it concisely; and we used a probabilistic programming system [13] with programmable inference [32] to manage the complexity of our inference and learning algorithm implementations. The current work has several limitations: Our algorithm runs $\approx 20x$ slower than the DenseFusion baseline. Our shape-learning algorithm requires that the training scenes contain only the single novel object, whose identity is known across training frames. Adding the ability to segment and learn models of novel objects in cluttered scenes and automatically train object detectors and pose estimators for these objects from short RGB-D video sequences, is an ongoing direction of work. The model also does not yet incorporate some important prior knowledge about scenes—interpenetration of objects is permitted, and constraints on physical stability are not incorporated. More experiments are also needed to understand the implications of a Bayesian treatment of 3D scene perception.

Scene Type	Object Type	# of Scenes	0.5cm Threshold				1.0cm Threshold				2.0cm Threshold			
			Accuracy				Accuracy				Accuracy			
			3DP3	3DP3*	DF	R6D	3DP3	3DP3*	DF	R6D	3DP3	3DP3*	DF	R6D
Single Object	002_master_chef_can	94	0.99	0.95	0.45	0.03	1.00	1.00	0.69	0.46	1.00	1.00	1.00	0.98
	003_cracker_box	92	0.55	0.39	0.16	0.00	0.98	0.98	0.39	0.02	1.00	1.00	0.78	0.42
	004_sugar_box	109	0.90	0.87	0.17	0.00	1.00	1.00	0.72	0.32	1.00	1.00	1.00	1.00
	005_tomato_soup_can	108	0.88	0.81	0.18	0.00	1.00	1.00	0.36	0.07	1.00	1.00	0.86	0.74
	006_mustard_bottle	97	0.86	0.79	0.48	0.01	1.00	1.00	0.57	0.36	1.00	1.00	0.81	0.89
Stacked	002_master_chef_can	190	0.86	0.79	0.28	0.02	0.94	0.93	0.56	0.39	0.95	0.95	1.00	0.98
	003_cracker_box	204	0.41	0.24	0.16	0.00	0.85	0.81	0.41	0.04	0.97	0.96	0.76	0.40
	004_sugar_box	214	0.63	0.61	0.14	0.01	0.92	0.91	0.61	0.33	0.94	0.94	0.99	0.99
	005_tomato_soup_can	193	0.67	0.52	0.13	0.00	0.89	0.86	0.28	0.06	0.90	0.88	0.75	0.66
	006_mustard_bottle	199	0.73	0.60	0.44	0.03	0.94	0.90	0.54	0.30	0.94	0.94	0.85	0.88
Partial View	002_master_chef_can	106	0.81	0.80	0.11	0.00	1.00	1.00	0.30	0.04	1.00	1.00	0.67	0.42
	003_cracker_box	99	0.18	0.16	0.00	0.00	0.60	0.57	0.01	0.00	0.82	0.80	0.14	0.04
	004_sugar_box	111	0.63	0.59	0.00	0.00	0.89	0.89	0.08	0.04	1.00	1.00	0.73	0.68
	005_tomato_soup_can	87	0.34	0.33	0.00	0.00	0.72	0.71	0.13	0.00	0.83	0.82	0.40	0.13
	006_mustard_bottle	97	0.55	0.62	0.08	0.00	0.87	0.86	0.23	0.00	0.96	0.95	0.37	0.26
Partially Occluded	002_master_chef_can	130	0.71	0.52	0.04	0.00	0.93	0.90	0.13	0.02	0.99	0.99	0.22	0.12
	003_cracker_box	500	0.37	0.35	0.59	0.00	1.00	1.00	1.00	0.02	1.00	1.00	1.00	1.00
	004_sugar_box	117	0.02	0.01	0.06	0.00	0.30	0.27	0.40	0.12	0.94	0.93	0.84	0.77
	005_tomato_soup_can	124	0.04	0.00	0.01	0.00	0.31	0.23	0.14	0.06	0.81	0.75	0.50	0.49
	006_mustard_bottle	129	0.70	0.43	0.55	0.03	0.84	0.74	0.95	0.29	0.94	0.90	1.00	0.99

Table 2: Accuracy results on our synthetic YCB-Challenging data set. We report the number of scenes over which this accuracy is computed for each object and scene type. Accuracy is shown for 3DP3 and 3DP3*, which are our full method and an ablation that does not model contact relationships, respectively, and two deep learning baselines (DenseFusion (DF) [42] and Robust6D (R6D) [39]).

Scene Type	Method	Tomato Soup			Cracker Box			Potted Meat			Sugar Box			Master Chef		
		ADD-S			ADD-S			ADD-S			ADD-S			ADD-S		
		Q1	Q2	Q3												
Single object	3DP3 (ours)	0.35	0.39	0.41	0.43	0.49	0.54	0.36	0.40	0.45	0.38	0.43	0.48	0.37	0.43	0.48
	3DP3* (ours)	0.35	0.40	0.43	0.47	0.52	0.62	0.36	0.39	0.44	0.40	0.45	0.49	0.35	0.41	0.49
	DenseFusion	0.35	0.55	1.11	0.65	1.35	1.72	0.58	0.88	1.02	0.67	1.25	1.72	0.32	0.61	1.85
	Robust6D	0.84	1.05	1.29	1.65	2.22	2.90	0.97	1.09	1.21	1.25	1.61	2.02	0.83	1.48	1.89
Stacked	3DP3 (ours)	0.37	0.42	0.46	0.46	0.52	0.60	0.39	0.45	0.60	0.40	0.46	0.52	0.40	0.45	0.51
	3DP3* (ours)	0.38	0.42	0.48	0.50	0.60	0.79	0.40	0.46	0.64	0.43	0.49	0.61	0.41	0.47	0.56
	DenseFusion	0.49	0.87	1.21	0.66	1.33	1.97	0.63	0.92	1.16	0.93	1.42	1.96	0.37	0.66	1.83
	Robust6D	0.84	1.15	1.36	1.68	2.21	2.86	0.92	1.11	1.26	1.37	1.72	2.21	0.94	1.38	1.82
Partial view	3DP3 (ours)	0.34	0.40	0.47	0.54	0.76	1.56	0.36	0.45	0.59	0.47	0.55	1.80	0.36	0.47	0.57
	3DP3* (ours)	0.33	0.40	0.47	0.56	0.90	1.54	0.37	0.45	0.63	0.46	0.59	1.81	0.36	0.46	0.58
	DenseFusion	0.79	1.52	2.10	2.33	2.93	3.81	1.26	1.65	2.07	1.52	2.14	3.78	1.05	2.22	2.71
	Robust6D	1.43	2.25	2.93	3.40	4.03	4.77	1.51	1.83	2.13	2.24	2.99	4.30	1.97	2.50	3.27
Partially Occluded	3DP3 (ours)	0.36	0.42	0.52	0.48	0.52	0.55	0.91	1.25	1.57	0.89	1.69	1.97	0.36	0.42	0.55
	3DP3* (ours)	0.39	0.49	0.64	0.48	0.53	0.58	0.97	1.29	1.66	1.03	1.72	1.99	0.43	0.58	1.01
	DenseFusion	-	-	-	0.41	0.48	0.58	0.81	1.11	1.53	1.47	2.01	3.18	0.38	0.48	0.64
	Robust6D	-	-	-	1.30	1.48	1.61	1.15	1.46	1.87	1.48	2.02	3.24	0.94	1.10	1.33

Table 3: Robustness of inference. We quantify the ADD-S error at 1st, 2nd, and 3rd quartiles for each scene type and object type in the synthetic dataset of hard scenes. A value of - indicates the method made no prediction for the object’s pose. 3DP3* denotes an ablated version of our method without inference of the scene graph structure and thus object-object contact.

8 Acknowledgements

The authors acknowledge Javier Felip Leon (Intel) for helpful discussions and a prototype depth renderer, and Omesh Tickoo (Intel) for helpful discussions. This work was funded in part by the DARPA Machine Common Sense program (Award ID: 030523-00001); by the Singapore DSTA / MIT SCC collaboration; by Intel’s Probabilistic Computing Center; and by philanthropic gifts from the Aphorism Foundation and the Siegel Family Foundation. We thank Alex Lew, Tan Zhi-Xuan, Feras Saad, Cameron Freer, McCoy Becker, Sam Witty, and George Matheos for helpful feedback.

References

- [1] Sameer Agarwal, Noah Snavely, Steven M Seitz, and Richard Szeliski. Bundle Adjustment in the Large. In *ECCV 2010: Proceedings of the European Conference on Computer Vision*, pages 29–42. Springer, 2010.
- [2] Christophe Andrieu, Gareth O Roberts, et al. The pseudo-marginal approach for efficient Monte Carlo computations. *The Annals of Statistics*, 37(2):697–725, 2009.
- [3] Iro Armeni, Zhi-Yang He, JunYoung Gwak, Amir R Zamir, Martin Fischer, Jitendra Malik, and Silvio Savarese. 3D Scene Graph: A Structure for Unified Semantics, 3D Space, and Camera. In *ICCV 2019: Proceedings of the IEEE/CVF International Conference on Computer Vision*, pages 5664–5673, 2019.
- [4] Jonathan Baldwin. Hopf Fibration. Available at https://vrs.amsi.org.au/wp-content/uploads/sites/78/2017/05/baldwin_jonathan_vrs-report.pdf (2021/06/04).
- [5] Sid Yingze Bao and Silvio Savarese. Semantic structure from motion. In *CVPR 2011: Proceedings of the IEEE Conference on Computer Vision and Pattern Recognition*, pages 2025–2032. IEEE, 2011.
- [6] Paul J Besl and Neil D McKay. Method for registration of 3D shapes. In *Sensor Fusion IV: Control Paradigms and Data Structures*, volume 1611, pages 586–606. International Society for Optics and Photonics, 1992.
- [7] Berk Calli, Aaron Walsman, Arjun Singh, Siddhartha Srinivasa, Pieter Abbeel, and Aaron M. Dollar. Benchmarking in Manipulation Research: Using the Yale-CMU-Berkeley Object and Model Set. *IEEE Robotics Automation Magazine*, 22(3):36–52, 2015.
- [8] Arthur Cayley. *A Theorem on Trees*, volume 13 of *Cambridge Library Collection - Mathematics*, page 26–28. Cambridge University Press, 2009.
- [9] Xiaotong Chen, Rui Chen, Zhiqiang Sui, Zhefan Ye, Yanqi Liu, R Iris Bahar, and Odest Chadwicke Jenkins. GRIP: Generative Robust Inference and Perception for Semantic Robot Manipulation in Adversarial Environments. In *IROS 2019: IEEE/RSJ International Conference on Intelligent Robots and Systems*, pages 3988–3995. IEEE, 2019.
- [10] Yixin Chen, Siyuan Huang, Tao Yuan, Siyuan Qi, Yixin Zhu, and Song-Chun Zhu. Holistic++ Scene Understanding: Single-view 3D Holistic Scene Parsing and Human Pose Estimation with Human-Object Interaction and Physical Commonsense. In *ICCV 2019: Proceedings of the IEEE/CVF International Conference on Computer Vision*, pages 8648–8657, 2019.
- [11] James H. Clark. Hierarchical Geometric Models for Visible Surface Algorithms. *Commun. ACM*, 19(10):547–554, October 1976.
- [12] Marco Cusumano-Towner, Alexander K Lew, and Vikash K Mansinghka. Automating Involutive MCMC using Probabilistic and Differentiable Programming. *arXiv preprint arXiv:2007.09871*, 2020.
- [13] Marco F Cusumano-Towner, Feras A Saad, Alexander K Lew, and Vikash K Mansinghka. Gen: A General-Purpose Probabilistic Programming System with Programmable Inference. In *PLDI 2019: Proceedings of the 40th ACM SIGPLAN Conference on Programming Language Design and Implementation*, pages 221–236, 2019.
- [14] Fei Deng, Zhuo Zhi, and Sungjin Ahn. Generative Hierarchical Models for Parts, Objects, and Scenes. *arXiv preprint arXiv:1910.09119*, 2019.
- [15] Fei Deng, Zhuo Zhi, Donghun Lee, and Sungjin Ahn. Generative Scene Graph Networks. In *ICLR 2021: International Conference on Learning Representations*, 2021.
- [16] Xinke Deng, Arsalan Mousavian, Yu Xiang, Fei Xia, Timothy Bretl, and Dieter Fox. PoseRBPF: A Rao-Blackwellized Particle Filter for 6-D Object Pose Tracking. *IEEE Transactions on Robotics*, 2021.
- [17] Karthik Desingh, Shiyang Lu, Anthony Opipari, and Odest Chadwicke Jenkins. Efficient nonparametric belief propagation for pose estimation and manipulation of articulated objects. *Science Robotics*, 4(30):eaaw4523, 2019.
- [18] Yilun Du, Zhijian Liu, Hector Basevi, Ales Leonardis, Bill Freeman, Josh Tenenbaum, and Jiajun Wu. Learning to Exploit Stability for 3D Scene Parsing. In S. Bengio, H. Wallach,

- H. Larochelle, K. Grauman, N. Cesa-Bianchi, and R. Garnett, editors, *NIPS 2018: Advances in Neural Information Processing Systems*, volume 31. Curran Associates, Inc., 2018.
- [19] SM Eslami, Nicolas Heess, Theophane Weber, Yuval Tassa, David Szepesvari, Geoffrey E Hinton, et al. Attend, Infer, Repeat: Fast Scene Understanding with Generative Models. *NIPS 2016: Advances in Neural Information Processing Systems*, 29:3225–3233, 2016.
- [20] Jean Gallier. *The Quaternions and the Spaces S^3 , $SU(2)$, $SO(3)$, and RP^3* , pages 248–266. Springer New York, New York, NY, 2001.
- [21] Dileep George, Wolfgang Lehrach, Ken Kansky, Miguel Lázaro-Gredilla, Christopher Laan, Bhaskara Marthi, Xinghua Lou, Zhaoshi Meng, Yi Liu, Huayan Wang, Alex Lavin, and D. Scott Phoenix. A generative vision model that trains with high data efficiency and breaks text-based captchas. *Science*, 358(6368):eaag2612, 2017.
- [22] Jared Glover, Gary Bradski, and Radu Bogdan Rusu. Monte Carlo Pose Estimation with Quaternion Kernels and the Bingham Distribution. In *RSS 2012: Robotics: Science and Systems*, volume 7, page 97, 2012.
- [23] Tomáš Hodaň, Frank Michel, Eric Brachmann, Wadim Kehl, Anders Glent Buch, Dirk Kraft, Bertram Drost, Joel Vidal, Stephan Ihrke, Xenophon Zabulis, Caner Sahin, Fabian Manhardt, Federico Tombari, Tae-Kyun Kim, Jiří Matas, and Carsten Rother. BOP: Benchmark for 6D object pose estimation. *ECCV 2018: Proceedings of the European Conference on Computer Vision*, 2018.
- [24] Siyuan Huang, Siyuan Qi, Yixin Zhu, Yinxue Xiao, Yuanlu Xu, and Song-Chun Zhu. Holistic 3D scene parsing and reconstruction from a single RGB image. In *ECCV 2018: Proceedings of the European Conference on Computer Vision*, pages 187–203, 2018.
- [25] D Knill D Kersten and A Yuille. Introduction: A Bayesian Formulation of Visual Perception. *Perception as Bayesian inference*, pages 1–21, 1996.
- [26] Daniel Kersten, Pascal Mamassian, and Alan Yuille. Object Perception as Bayesian Inference. *Annu. Rev. Psychol.*, 55:271–304, 2004.
- [27] Nilesh Kulkarni, Ishan Misra, Shubham Tulsiani, and Abhinav Gupta. 3D-RelNet: Joint object and relational network for 3D prediction. In *Proceedings of the IEEE/CVF International Conference on Computer Vision*, pages 2212–2221, 2019.
- [28] Tejas D Kulkarni, Pushmeet Kohli, Joshua B Tenenbaum, and Vikash Mansinghka. Picture: A Probabilistic Programming Language for Scene Perception. In *CVPR 2015: Proceedings of the IEEE Conference on Computer Vision and Pattern Recognition*, pages 4390–4399, 2015.
- [29] J.M. Lee. *Introduction to Smooth Manifolds*. Graduate Texts in Mathematics. Springer, 2003.
- [30] Tai Sing Lee and David Mumford. Hierarchical Bayesian Inference in the Visual Cortex. *JOSA A*, 20(7):1434–1448, 2003.
- [31] Vikash K Mansinghka, Tejas D Kulkarni, Yura N Perov, and Josh Tenenbaum. Approximate Bayesian Image Interpretation using Generative Probabilistic Graphics Programs. *NIPS 2013: Advances in Neural Information Processing Systems*, 26:1520–1528, 2013.
- [32] Vikash K Mansinghka, Ulrich Schaechtle, Shivam Handa, Alexey Radul, Yutian Chen, and Martin Rinard. Probabilistic Programming with Programmable Inference. In *PLDI 2018: Proceedings of the 39th ACM SIGPLAN Conference on Programming Language Design and Implementation*, pages 603–616, 2018.
- [33] Ben Mildenhall, Pratul P Srinivasan, Matthew Tancik, Jonathan T Barron, Ravi Ramamoorthi, and Ren Ng. NeRF: Representing Scenes as Neural Radiance Fields for View Synthesis. In *ECCV 2020: Proceedings of the European Conference on Computer Vision*, pages 405–421. Springer, 2020.
- [34] Pol Moreno, Christopher KI Williams, Charlie Nash, and Pushmeet Kohli. Overcoming Occlusion with Inverse Graphics. In *ECCV 2016: Proceedings of the European Conference on Computer Vision*, pages 170–185. Springer, 2016.
- [35] Lukasz Romaszko, Christopher K. I. Williams, Pol Moreno, and Pushmeet Kohli. Vision-as-Inverse-Graphics: Obtaining a Rich 3D Explanation of a Scene from a Single Image. In *ICCVW 2017: IEEE International Conference on Computer Vision Workshops*, pages 940–948, 2017.

- [36] Antoni Rosinol, Arjun Gupta, Marcus Abate, Jingnan Shi, and Luca Carlone. 3D Dynamic Scene Graphs: Actionable Spatial Perception with Places, Objects, and Humans. *arXiv preprint arXiv:2002.06289*, 2020.
- [37] Ruwen Schnabel, Roland Wahl, and Reinhard Klein. Efficient RANSAC for point-cloud shape detection. In *Computer graphics forum*, volume 26, pages 214–226. Wiley Online Library, 2007.
- [38] Johannes L. Schönberger and Jan-Michael Frahm. Structure-from-Motion Revisited. In *CVPR 2016: IEEE Conference on Computer Vision and Pattern Recognition*, pages 4104–4113, 2016.
- [39] Meng Tian, Liang Pan, Marcelo H Ang Jr, and Gim Hee Lee. Robust 6D Object Pose Estimation by Learning RGB-D Features. In *ICRA 2020: International Conference on Robotics and Automation*, 2020.
- [40] Jonathan Tremblay, Thang To, Balakumar Sundaralingam, Yu Xiang, Dieter Fox, and Stan Birchfield. Deep Object Pose Estimation for Semantic Robotic Grasping of Household Objects. In *CORL 2018: Conference on Robot Learning*, 2018.
- [41] Zhuowen Tu and Song-Chun Zhu. Image segmentation by data-driven Markov chain Monte Carlo. *IEEE Transactions on Pattern Analysis and Machine Intelligence*, 24(5):657–673, 2002.
- [42] Chen Wang, Danfei Xu, Yuke Zhu, Roberto Martín-Martín, Cewu Lu, Li Fei-Fei, and Silvio Savarese. DenseFusion: 6D Object Pose Estimation by Iterative Dense Fusion. In *CVPR 2019: Proceedings of the IEEE/CVF Conference on Computer Vision and Pattern Recognition*, pages 3343–3352, 2019.
- [43] Yu Xiang, Tanner Schmidt, Venkatraman Narayanan, and Dieter Fox. PoseCNN: A Convolutional Neural Network for 6D Object Pose Estimation in Cluttered Scenes. 2018.
- [44] Anna Yershova, Swati Jain, Steven M. LaValle, and Julie C. Mitchell. Generating Uniform Incremental Grids on SO(3) Using the Hopf Fibration. *The International Journal of Robotics Research*, 29(7):801–812, 2010.
- [45] Alan Yuille and Daniel Kersten. Vision as Bayesian Inference: Analysis by Synthesis? *Trends in Cognitive Sciences*, 10(7):301–308, 2006.
- [46] Song Chun Zhu and Alan Yuille. Region competition: Unifying snakes, region growing, and bayes/mdl for multiband image segmentation. *IEEE Transactions on Pattern Analysis and Machine Intelligence*, 18(9):884–900, 1996.
- [47] Ben Zinberg, Marco Cusumano-Towner, and K Mansinghka Vikash. Structured differentiable models of 3D scenes via generative scene graphs. In *Workshop on Perception as Generative Reasoning, NeurIPS 2019, Vancouver, Canada*, 2019.

A Broader Impact

While the goal of robust scene parsing and pose estimation is challenging, and the present work is an early step with much more work lying ahead, it is important to consider potential societal impacts of this work, both positive and negative. Robust pose estimation will be instrumental in improving the reliability of a wide variety of applications—including assistive technologies for people with limited mobility, improved fault detection in manufacturing plants, and safer autopilot for autonomous vehicles. On the other hand, these same technologies, if used toward the wrong ends, could have negative societal impacts as well, such as unjust or inequitable surveillance, or weapon guidance systems that fall into the wrong hands. Even applications that are largely beneficial must be implemented thoughtfully to avoid negative side effects. For example, in the present work, the choice of prior distribution on contact structures implies an inductive bias that, if chosen incorrectly, could lead to technologies that are less reliable when the scene being parsed contains a person in a wheelchair. As a scientific community, it is important that we place continued emphasis on developing technical safeguards against both overt misuse and unintended consequences like the above. Furthermore, we must remember that technical safeguards on their own are not sufficient: we must communicate to broader society not just the benefits, but also the risks of this technology, so that users can be informed participants and apply this technology towards a better world.

B Pose estimation from synthetic RGB images

In the previous two sections, 3DP3 was used with a depth-rendering-based likelihood on depth images since an RGB-D image was given as input. In this section, we show that 3DP3 can be used to do pose estimation without depth data i.e. from just an RGB image. Instead of a depth likelihood, we substitute an RGB renderer and simple color likelihood. We qualitatively compare with Attend, Infer, Repeat (AIR) [19], an amortized inference approach based on recurrent neural networks which can be applied to infer poses of 3D objects. We generated scenes that resemble the tabletop scenes on which AIR qualitatively assessed pose inference accuracy. Figure 6 shows pairs of input RGB images and corresponding reconstructions from pose inferences made by 3DP3. Qualitatively, our system produces pose inferences of better or equal accuracy to AIR. Importantly, our system does not require training. In contrast, AIR takes approximately 3 days for training to converge. Also at these lower resolutions, our inference can run in 0.5s per frame.

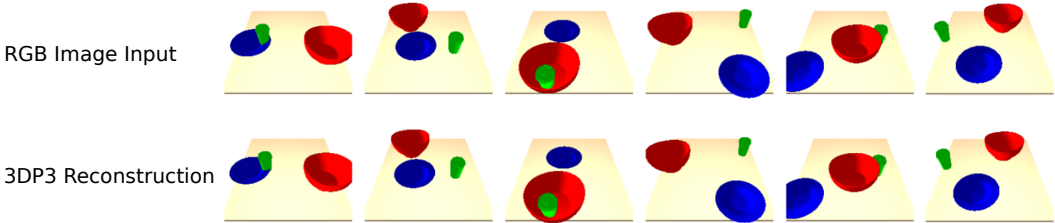


Figure 6: A variant of our scene graph inference algorithm that uses a RGB-based likelihood applied to synthetic RGB scenes designed to resemble those used in the evaluation of AIR [19]. Our algorithm gives accurate reconstructions with 0.5 seconds of inference time on these scenes and no training.

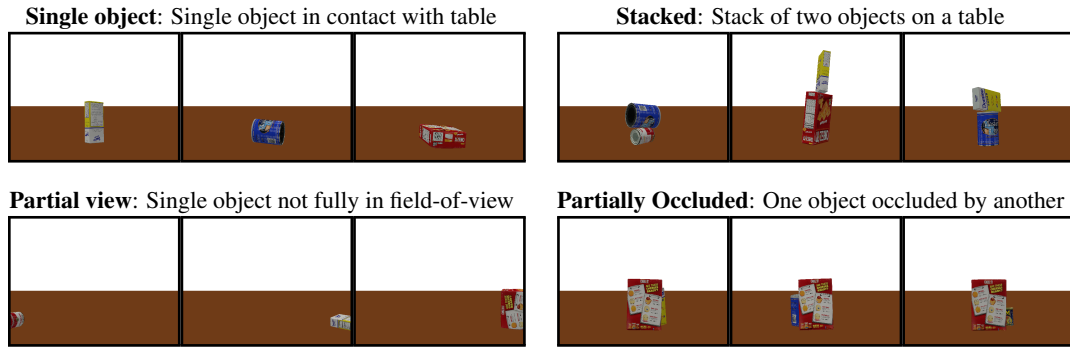
C Shape Learning Accuracy Quantitative Evaluation

Object Type	IoU
002_master_chef_can	0.9544
003_cracker_box	0.9716
004_sugar_box	0.9484
005_tomato_soup_can	0.9433
006_mustard_bottle	0.9671
007_tuna_fish_can	0.9696
008_pudding_box	0.9617
009_gelatin_box	0.9451
010_potted_meat_can	0.9654
011_banana	0.9599
019_pitcher_base	0.9808
021_bleach_cleanser	0.9582
024_bowl	0.9694
025_mug	0.9621
035_power_drill	0.966
036_wood_block	0.9679
037_scissors	0.9505
040_large_marker	0.9767
051_large_clamp	0.9218
052_extra_large_clamp	0.9228
061_foam_brick	0.9405

Table 4: We include a quantitative evaluation comparing the learned shape models to the ground truth shape models. To get a shape model from the learned shape prior, we take all voxels which the prior says are more likely to be occupied than unoccupied and compute the IoU between that volume and the ground truth object volume.

D YCB-Challenging Dataset

YCB-Challenging is a synthetic test dataset of 2000 RGB-D images, 500 in each of the following 4 categories:



E YCB-Challenging Extended Experimental Results

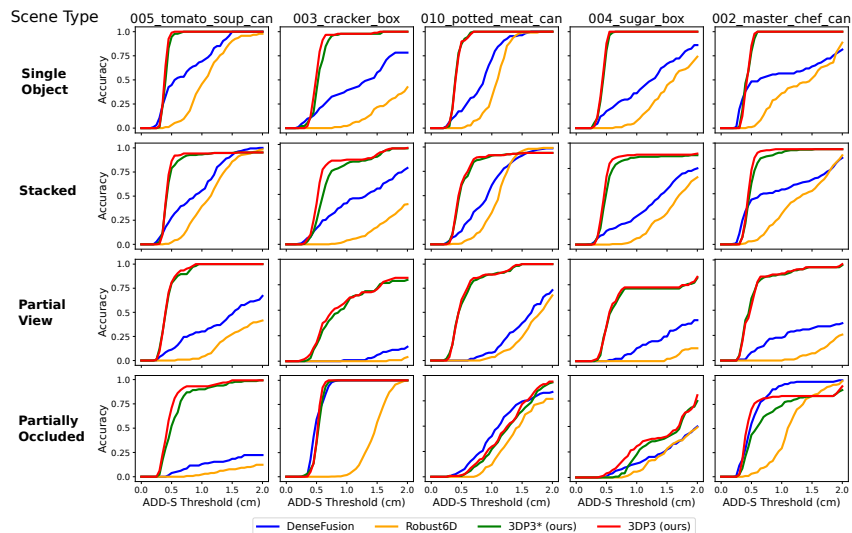


Figure 7: Accuracy of our method and two deep learning baselines (DenseFusion [42] and Robust6D [39]) on the task of 6DoF pose estimation in our synthetic ‘YCB-Challenging’ dataset. For each of the 4 scene types (rows) and 5 object types (columns), we measure accuracy for a range of ADD-S thresholds. 3DP3* denotes an ablated version of our method without inference of the scene graph structure and thus object-object contact (i.e. we fix the scene graph to G_0)

F YCB-Video Dataset

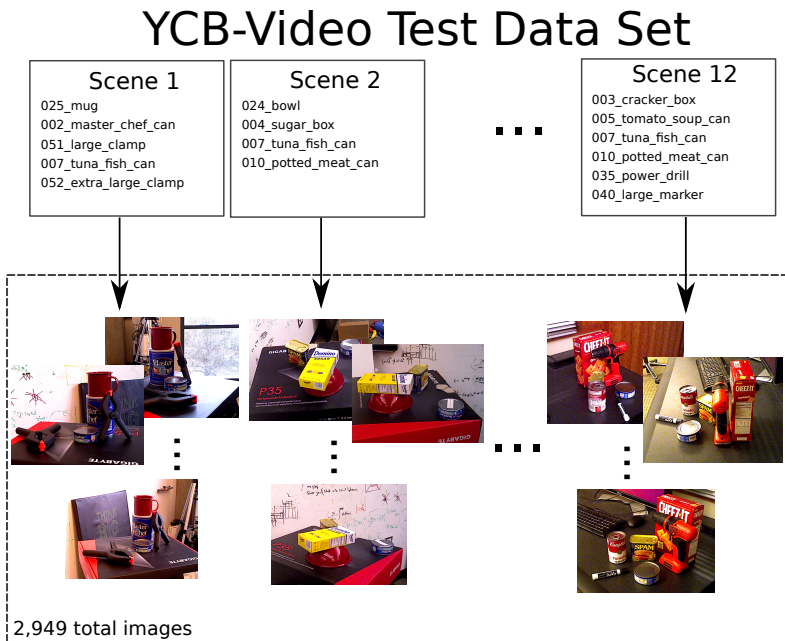


Figure 8: The YCB-Video [7] test data set consists of 2,949 real RGB-D images featuring the 21 YCB objects. These 2,949 images are collected from videos of 12 different scenes where the camera pans around the scene to view it from different perspectives. The 12 scenes contain different subsets of the 21 YCB objects, and some objects appear in multiple scenes (e.g 007_tuna_fish_can appears in Scenes 1, 2, and 12).

G Ablation Qualitative Results on YCB-Video

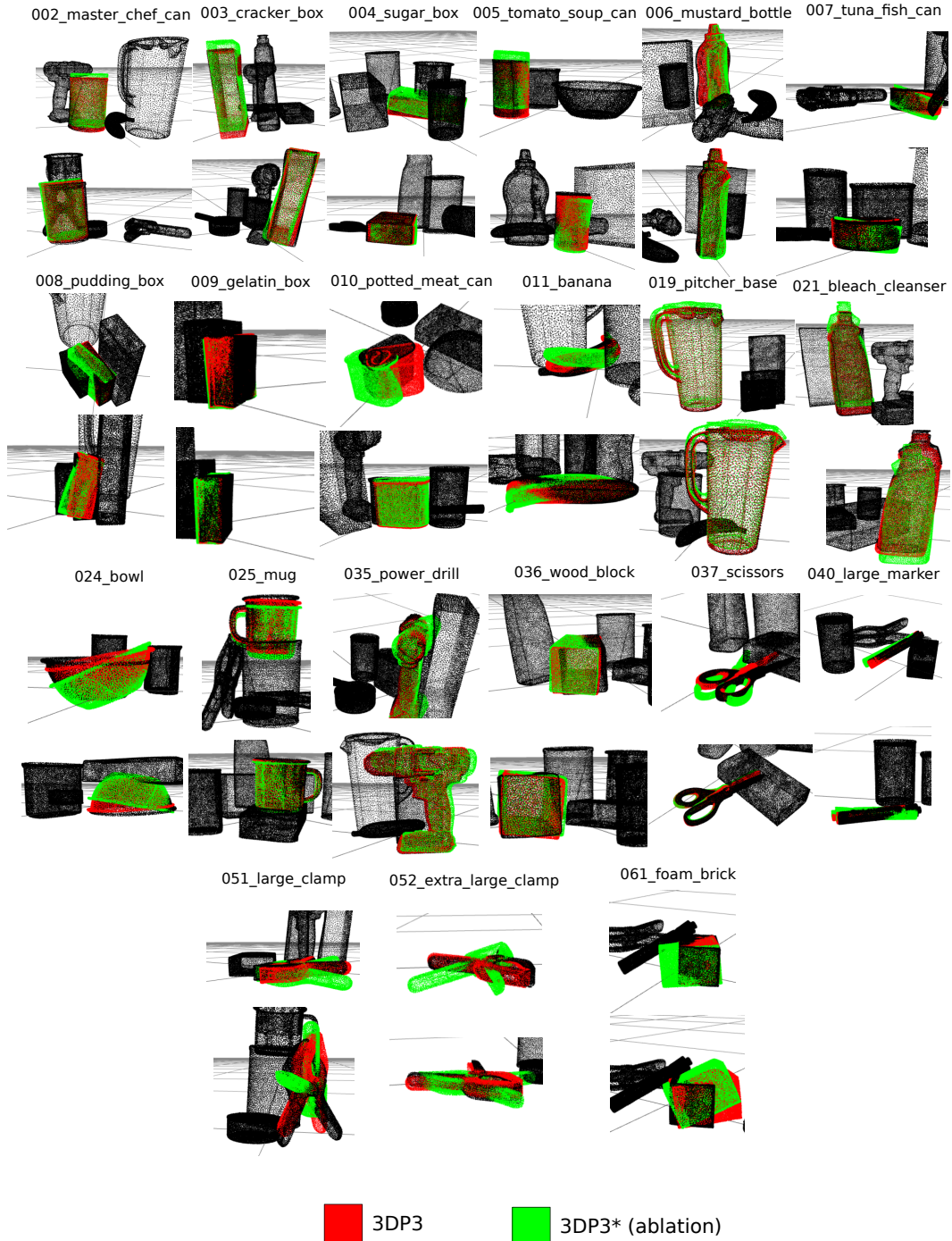


Figure 9: Comparison with ablated model on YCB-V real scenes. For each of the 21 YCB objects, we show 2 images of scenes containing that object and the poses estimated by our full method (3DP3) and an ablated version of our method (3DP3*) that does not model contact relationships.

H Qualitative Results on YCB-Video



Figure 10: YCB frames for each object, overlaid with pose estimates of DenseFusion (cyan) and 3DP3 (green), where there is a large performance difference between the two methods.

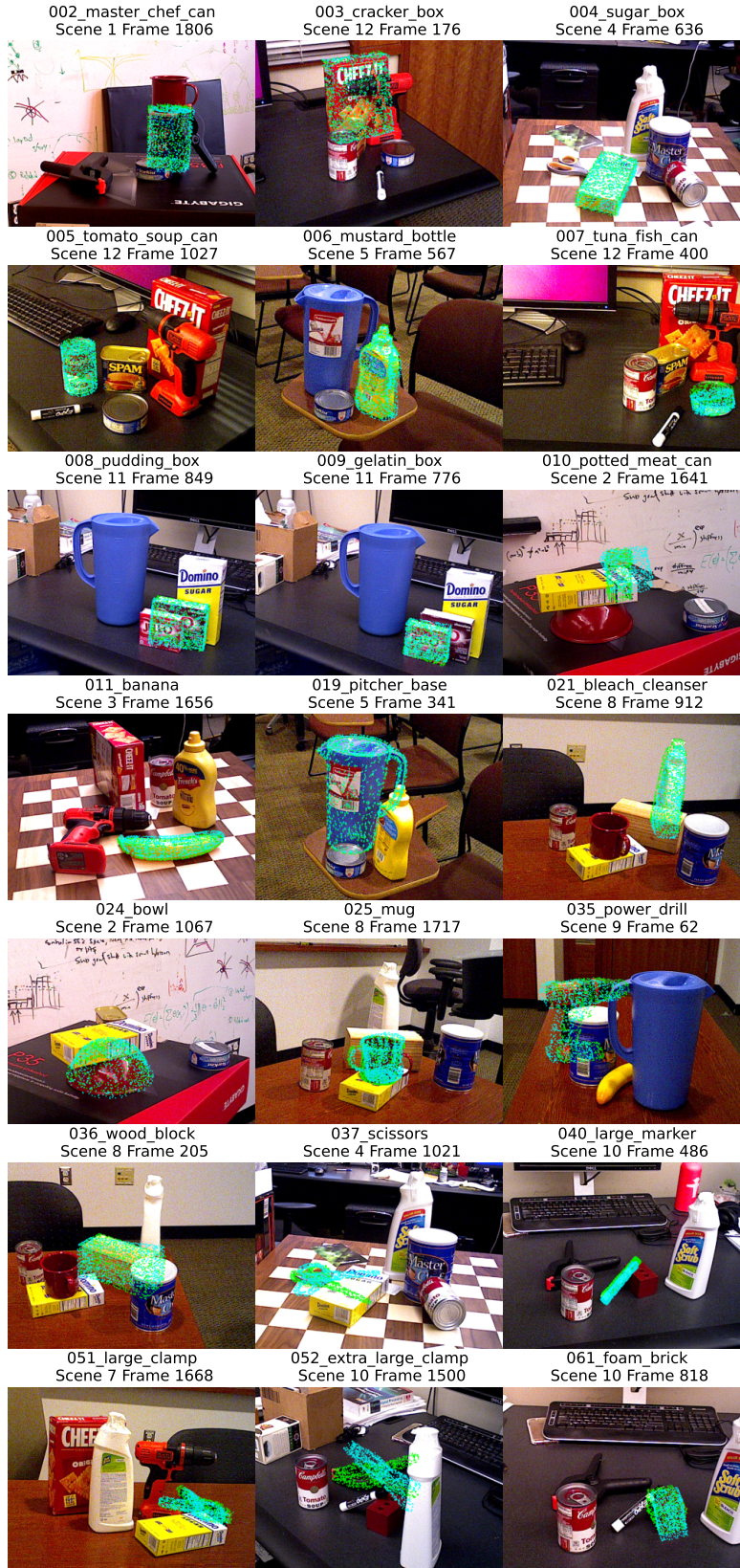


Figure 11: YCB frames for each object, overlaid with pose estimates of DenseFusion (cyan) and 3DP3 (green), where there is almost no performance difference between the two methods.

I Distilling shape distributions via variational inference

Recall that:

$$p'(\mathbf{O}|\mathbf{I}_{1:T}) = \sum_{k=1}^K w_k p'(\mathbf{O}|\mathbf{M}^{(k)}, \mathbf{x}_{1:T}^{(k)}, \mathbf{I}_{1:T}) \quad (3)$$

Consider the following variational family:

$$q_\varphi(\mathbf{O}) := \prod_{i \in [h]} \prod_{j \in [w]} \prod_{\ell \in [l]} \varphi_{ij\ell}^{O_{ij\ell}} \cdot (1 - \varphi_{ij\ell})^{(1-O_{ij\ell})} \quad (4)$$

where each $0 \leq \varphi_{ij\ell} \leq 1$ can be interpreted as a per-voxel occupancy probability. Then

$$\text{KL}(p'(\mathbf{O}|\mathbf{I}_{1:T})||q_\varphi(\mathbf{O})) = \mathbb{E}_{\mathbf{O} \sim p'(\cdot|\mathbf{I}_{1:T})} \left[\log \frac{p'(\mathbf{O}|\mathbf{I}_{1:T})}{q_\varphi(\mathbf{O})} \right]$$

Note that minimizing this KL divergence with respect to φ is equivalent to maximizing the following quantity:

$$\begin{aligned} & \mathbb{E}_{\mathbf{O} \sim p'(\cdot|\mathbf{I}_{1:T})} [\log q_\varphi(\mathbf{O})] \\ &= \sum_{k=1}^K w_k \mathbb{E}_{\mathbf{O} \sim p'(\cdot|\mathbf{M}^{(k)}, \mathbf{x}_{1:T}^{(k)}, \mathbf{I}_{1:T})} [\log q_\varphi(\mathbf{O})] \\ &= \sum_{k=1}^K w_k \mathbb{E}_{\mathbf{O} \sim p'(\cdot|\mathbf{M}^{(k)}, \mathbf{x}_{1:T}^{(k)}, \mathbf{I}_{1:T})} \left[\sum_{i \in [h]} \sum_{j \in [w]} \sum_{\ell \in [l]} \log q_\varphi(O_{ij\ell}) \right] \\ &= \sum_{k=1}^K w_k \mathbb{E}_{\mathbf{O} \sim p'(\cdot|\mathbf{M}^{(k)}, \mathbf{x}_{1:T}^{(k)}, \mathbf{I}_{1:T})} \left[\sum_{i \in [h]} \sum_{j \in [w]} \sum_{\ell \in [l]} O_{ij\ell} \log \varphi_{ij\ell} + (1 - O_{ij\ell}) \log(1 - \varphi_{ij\ell}) \right] \\ &= \sum_{i \in [h]} \sum_{j \in [w]} \sum_{\ell \in [l]} \sum_{k=1}^K w_k p'(O_{ij\ell} = 1|\mathbf{M}^{(k)}, \mathbf{x}_{1:T}^{(k)}, \mathbf{I}_{1:T}) \log \varphi_{ij\ell} + p'(O_{ij\ell} = 0|\mathbf{M}^{(k)}, \mathbf{x}_{1:T}^{(k)}, \mathbf{I}_{1:T}) \log(1 - \varphi_{ij\ell}) \end{aligned}$$

The optimization decomposes into separate problems for each $\varphi_{ij\ell}$, with global optimum:

$$\varphi_{ij\ell}^* = \sum_{k=1}^K w_k p'(O_{ij\ell} = 1|\mathbf{M}^{(k)}, \mathbf{x}_{1:T}^{(k)}, \mathbf{I}_{1:T})$$

J Probabilistic SLAM using Sequential Monte Carlo

To infer the camera poses $\mathbf{x}_{1:T}$ corresponding to the sequence of T depth images, we implemented a probabilistic SLAM using Sequential Monte Carlo. We assume the depth images contain background, which can be mapped and used for localization between frames. (In our data, the object is placed in the center of a rectangular room with a floor, ceiling, and four walls.) We also assume that the camera is the same distance away from the object in all T images. Finally, in order to ensure a reference frame match between the learned object model and ground truth model (such that at test time, object pose estimates of our system can be compared to the ground truth object poses), we provide the initial pose of the object in the camera frame.

To perform SLAM, we initialize a set of K particles with the observation, camera pose, and implied map at $t = 1$. Then, we enumerate over the position and viewing angle at $t = 2$, given the map at $t = 1$, observation at $t = 2$, and a prior on the camera pose conditioned on the pose at $t = 1$, and compute scores for each pose. We then construct a Gaussian mixture proposal where each component is centered on a different pose and has weight corresponding to the normalized score computed by the enumeration. We step the particles forward to $t = 2$ with this proposal distribution. Then, for each of the particles, we update the map given the observations and inferred poses. We repeat this for all T timesteps, at which point we have K particles with inferred camera poses for each of the T timesteps.

The depth image likelihood $p'(\mathbf{I}_t|\mathbf{O}, \mathbf{M}, \mathbf{x}_t) = \delta_{d(\mathbf{O}, \mathbf{M}, \mathbf{x}_t)}(\mathbf{I}_t)$ where d is a depth rendering function.

K Pose initialization for Scene Graph Inference

In the first stage of our scene graph inference algorithm, we obtain initial estimates of the 6DoF object poses via maximum-a-posteriori (MAP) inference in a restricted variant of our model that assumes no edges between objects in the scene graph. We maintain a set of particles with each particle assigned to a different object, and we have at least one particle assigned to each object. Then, for each particle we apply Metropolis-Hastings (MH) kernels to pose of the object that the particle is assigned to. After applying these MH kernels, we resample the set of particles using their normalized weights. We repeat this process of applying the MH kernels and resampling for a fixed number of iterations (proportional to the number of objects). We construct the MH kernels for each object by using spatial clustering and iterative closest point (ICP) to compute a set of “high-quality” poses for each object type given the observed scene. We first apply DBSCAN to the set of points that are unexplained by the current hypothesized scene. Then we create a set of initial object pose hypotheses with translation selected from the C cluster centers output by DBSCAN and orientation selected from the set of 24 nominal orientations, for a total of $24 \cdot C$ poses. (The 24 orientations are the rotational symmetries of a cube.). Next, we refine these initial pose estimates using ICP. The ICP does not use the full object model, but rather renders the object at the hypothesized pose and computes the corresponding point cloud. We score the resulting pose estimates under the generative model and use the normalized weights to construct a mixture proposal that serves as the MH kernel.

In addition to the above MH kernel, we also experimented with kernels based on Boltzmann proposals where the Hamiltonian is determined by performing a 3D convolution of a mask with the observed point cloud. Such proposals can potentially be used as “compiled detectors” of the object models $\mathbf{O}_{1:M}$, enabling us to perform online object learning and scene parsing. This class of proposals takes the following general form:

1. Discretize the observation into a 3D grid Γ .
2. Given the object model \mathbf{O} , create k convolutional masks to be convolved with the grid. Each mask is meant to detect \mathbf{O} at a certain orientation. The candidate orientations are obtained from an appropriately fine geodesic grid on a sphere.
3. Slide each mask over Γ and calculate the convolution of the mask and Γ .
4. Fix $\beta > 0$, and propose a pose from a Boltzmann distribution with temperature β , where the Hamiltonian of each pose is given by the convolution of its associated mask with Γ .

We tried multiple approaches for deriving convolutional masks from objects models. Maximally informative and maximally correlated masks require us to solve ill-posed optimization problems. Small windows sampled from the object model are not informative. These masks can give good proposals when combined with expensive ensembling and outlier detection, but they are unsuitable for online settings. Our best results come from globally-sparse, locally-dense [37], randomly selected masks. These masks are computationally efficient to apply and give results that are qualitatively comparable to the ICP-based kernel, but the sampling distribution of the masks have high-variance. In future work, we plan to further investigate this class of proposals.

L Parsing scenes with fully occluded objects and number uncertainty

Consider the setting when the number of objects in the scene (N) is unknown a-priori. Possibilities for prior probability distributions on N ($p(N)$) include (i) an a-priori known number of objects N_0 (used in the experiments in Section 6), (ii) Binomial(N_0, p_{present}), which is induced by a prior belief that each of N_0 objects is present with probability p_{present} (used in experiments described in Supplement L), and (iii) Poisson(λ), which places no a-priori upper bound on the number of objects.

In this section, we apply our framework to do probabilistic inference about the 6DoF pose and presence or absence of a fully occluded object, and investigate the dynamics of these inferences as we vary the fraction of the volume in the scene that is occluded.

Suppose a robot is tasked with assembling a piece of furniture, performing maintenance on a vehicle, or retrieving something from the kitchen. In each of these cases, the robot has a strong prior expectation that some object (e.g. a tool, component, or kitchen item) is present in the environment. However, in complex cluttered real-world environments the target object is likely to be fully occluded

from the robot’s view. That target object may even be absent, especially in human-robot interactive task situations (e.g. the component or item is missing or misplaced). To perform rationally in such situations, the robot will need to generate possible poses of the object that are concordant with its *absence* from its visual field. Also, the robot must consider the possibility that the object is indeed not present, by weighing the lack of observed presence of the object against the prior expectations.

Prior Consider a scenario where there are $N_0 = M$ unique objects that may or may not be present in a scene (N_0 denotes the total number of object instances, and M denote the number of object types). Suppose that the prior probability that the object of type m is present with probability $p_{\text{pres}}^{(m)}$ for $m \in \{1, \dots, M\}$. Then, the prior $p(N, \mathbf{c})$ is:

$$p(N, \mathbf{c}) = \begin{cases} \frac{1}{N!} \prod_{m=1}^M p_{\text{pres}}^{(m) \mathbf{1}[m \in \mathbf{c}]} (1 - p_{\text{pres}}^{(m)})^{\mathbf{1}[m \notin \mathbf{c}]} & \text{if } |\mathbf{c}| = N \text{ and } \sum_{i=1}^N \mathbf{1}[c_i = m] \leq 1 \forall m \\ 0 & \text{otherwise} \end{cases} \quad (5)$$

In the special case when $p_{\text{pres}}^{(m)}$ is the same for all m (this is the case in our experiments below), we can write the marginal distribution $p(N)$ and conditional distribution $p(\mathbf{c}|N)$ as:

$$N \sim \text{Binomial}(M = N_0, p_{\text{pres}}) \quad (6)$$

and

$$p(\mathbf{c}|N) = \begin{cases} \frac{(M-N)!}{M!} & \text{if } |\mathbf{c}| = N \text{ and } \sum_{i=1}^N \mathbf{1}[c_i = m] \leq 1 \forall m \\ 0 & \text{otherwise} \end{cases} \quad (7)$$

For each possible (N, \mathbf{c}) , we fix the scene graph G to be the graph $G_0(N)$ on N vertices that has with no object-object edges:

$$p(G|N) = \begin{cases} 1 & \text{if } G = G_0(N) \\ 0 & \text{otherwise} \end{cases} \quad (8)$$

That is, each object v has an independent 6DoF pose \mathbf{x}_v . The prior distribution on the orientation component used the uniform distribution on an Euler angle parametrization, and the prior on the translation component (i.e. the location of the object) the uniform distribution on a cuboid volume representing the extent of the scene.

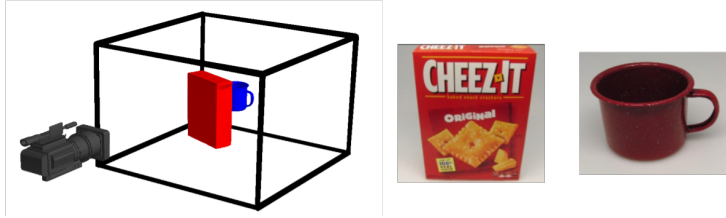
Likelihood Instead of the likelihood on point clouds used in Section 3.3, here we use an alternative likelihood based on (i) rendering a depth image $\tilde{\mathbf{I}}(\mathbf{O}_{1:M}, \mathbf{c}, G, \boldsymbol{\theta})$ and then (ii) adding noise to generate an observed depth image \mathbf{I} . The likelihood is a per-pixel mixture between a uniform distribution on the range of possible depth values, and a normal distribution with fixed variance σ^2 :

$$p(\mathbf{I}|x) = \prod_i \left(0.1 \cdot \frac{1}{D} + 0.9 \cdot \mathcal{N}(I_i; \tilde{I}_i, \sigma) \right)$$

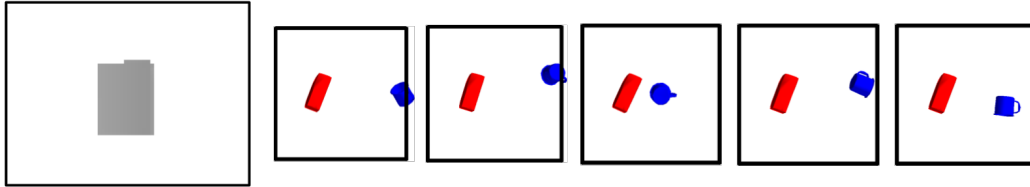
where i indexes pixels of the depth image. Pixels whose ray does not intersect an object are assigned the maximum depth value D . A similar likelihood function on depth images was used in [34].

MCMC inference algorithm We use a Markov chain Monte Carlo (MCMC) inference algorithm that cycles through each object type $m \in \{1, \dots, M\}$, and applies several types of MCMC moves for each type, based on the following proposals: (i) involutive MCMC kernels that switch an object type from being absent to being present and vice versa (proposing its pose from the prior), (ii) Metropolis–Hastings kernels that propose the translational components of the pose \mathbf{x}_v for each object from the prior, (iii) Metropolis–Hastings kernels that propose the rotational component of the pose for each object from the prior, and (iv) coordinate-wise random-walk proposals to each of the 6 dimensions of the pose of each object (the 3 coordinates of its location and its Euler angles). We initialize the Markov chain with a sample from the prior distribution.

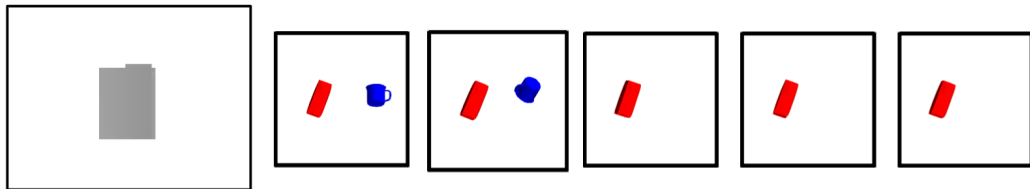
Inferring the 6DoF pose of a fully occluded object We first investigated inference about the 6DoF pose of an object (the mug from the YCB object set [7]) that is assumed to be in a volume in front of the camera, but that is not visible. This scenario arises when searching for a component or tool that is expected to be in the environment. Narrowing down where the object could be, based on observing where it is not, is important for efficiently planning and acting to obtain more information



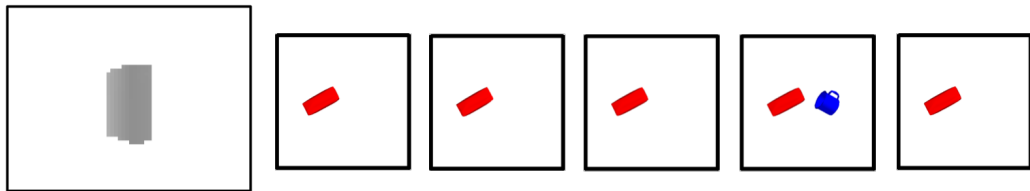
(a) The scenario (left). A depth camera is viewing a scene that may or may not contain a cracker box (middle) and a mug (right). We perform Bayesian inference on the existence and contingently, their 6DoF poses within the scene, of both objects. Only the cracker box is visible in the observed depth images (see below).



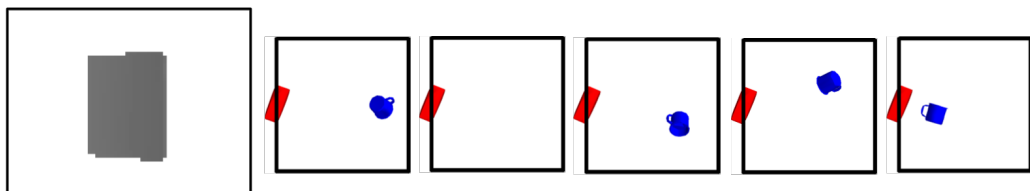
(b) Observed depth image and posterior samples where the existence of both the box and mug are assumed.



(c) Observed depth image and posterior samples where the existences of each object have prior probability 0.90. The posterior probabilities of existence for the mug and box are 0.37 and 1.0, respectively.



(d) Observed depth image and posterior samples where the existences of each object have prior probability 0.90. Note that the observed image has the box angled so that it occupies less of the field of view than in (c). The posterior probabilities of existence for the mug and box are 0.33 and 1.0, respectively.



(e) Observed depth image and posterior samples where the existences of each object have prior probability 0.90. Note that the observed image has the box closer to the camera, so that it occupies more of the field of view than in (c). The posterior probabilities of existence for the mug and box are 0.63 and 1.0, respectively.

Figure 12: Inferring the 6DoF pose and existence of multiple objects from depth images using MCMC in a generative model. Several scenarios are shown, with five approximate posterior samples from each. To estimate posterior probabilities of object existence, 20 posterior samples were used. The *lack of percept* of the mug in the visual field (i) reduces the posterior probability of its presence, but also (ii) informs the distribution on its 6DoF pose, if it is present. Note that as the fraction of volume in the scene that is occluded by the box decreases, the posterior probability that mug is present decreases.

and retrieve the object. In order for inference to be coherent, the lack of the object’s visible presence must be explained away by the occluding presence of another object. Therefore, we also assume the presence of another object (the cracker box). The results (Figure 12(b)) show that the algorithm successfully infer a variety of 6DoF poses of the mug in which it lies behind the cracker box.

Jointly inferring the existence and poses of multiple objects If an object is not visible, we may conclude that it is not present in the scene. The degree of belief in the presence of an object that is not visible depends on the degree of prior belief in its presence and the volume of possible states in which the object is fully occluded. If there are no other objects in the scene, then intuitively, there is nowhere the object could be hiding in the scene, so it must be absent. If there are other objects in the scene, then the pose of these other objects interacts with the object’s existence, in our beliefs. To investigate the interaction between the beliefs about the poses and existence of multiple objects, we generated synthetic depth data for several scenarios (Figure 12(c-e)). In all scenarios, the prior probabilities that the box and mug are present are both 0.9. In the first scenario (Figure 12(c)) the box is oriented so a wide face is facing the camera. We correctly infer the existence of the box with high confidence (1.0 posterior probability) and we assign 0.37 posterior probability to the existence of the mug. In the second scenario (Figure 12(d)) the box is rotated so that it occupies less of the camera’s field of view. As expected, this causes the posterior probability of the mug’s existence to decrease to 0.31. In the third scenario (Figure 12(e)), we move the box closer to the camera so that it occupies more of the field of view. The posterior probability of the mug’s presence then increases to 0.63. These experiments illustrate the dependence between one object’s pose and another object’s existence, which is a consequence of occlusion.

M Experiment Details

The deep learning baseline experiments were run on a 3.70GHz Intel i7 processor with 64GB RAM and a Nvidia GeForce GTX 1080Ti GPU. All other experiments were run a 2.40GHz Intel i9 processor with 32GB RAM and a Nvidia GeForce GTX 1650 Mobile GPU. Our model is implemented using Julia in Gen, a probabilistic programming system [13].

N Pseudomarginal shape inference

We use MH and involutive MCMC kernels that are stationary with respect to a target distribution on an extended state space that includes auxiliary variables $\mathbf{O}^{(i)}$ for $i = 1, \dots, R$ (R copies of all object shape models) by replacing the likelihood $p(\mathbf{Y}|N, \mathbf{c}, G', \boldsymbol{\theta}')$ for each proposed state in the acceptance probability with the following unbiased estimate obtained by sampling object models from the prior:

$$\frac{1}{R} \sum_{i=1}^R p(\mathbf{Y}|\mathbf{O}_1^{(i)}, \dots, \mathbf{O}_M^{(i)}, N, \mathbf{c}, G, \boldsymbol{\theta}) \text{ where } \mathbf{O}_c^{(i)} \stackrel{\text{i.i.d.}}{\sim} p(\cdot) \quad (9)$$

and replacing the likelihood in the denominator of the acceptance ratios with the unbiased estimate computed by the last accepted proposal. This is an instance of the pseudomarginal MCMC [2] framework. For example, for the scene graph involutive MCMC kernel described in Section O, each factor of the form:

$$\frac{p(\mathbf{Y}|N, \mathbf{c}, G', \boldsymbol{\theta}')}{p(\mathbf{Y}|N, \mathbf{c}, G, \boldsymbol{\theta})} \quad (10)$$

is replaced with a factor:

$$\frac{\frac{1}{R} \sum_{i=1}^R p(\mathbf{Y}|\mathbf{O}_1^{(i)'}, \dots, \mathbf{O}_M^{(i)'}, N, \mathbf{c}, \mathcal{G})}{\frac{1}{R} \sum_{i=1}^R p(\mathbf{Y}|\mathbf{O}_1^{(i)}, \dots, \mathbf{O}_M^{(i)}, N, \mathbf{c}, \mathcal{G})} \quad (11)$$

where the $\mathbf{O}_j^{(i)}$ are the shape models that were sampled when proposing the last state that was accepted, and where the $\mathbf{O}_j^{(i)'}$ are the shape models that are sampled during the current proposal. Note that the old sampled shape models $\mathbf{O}_j^{(i)}$ themselves do not need to be persisted across steps of the Markov chain—the only the denominator in the expression above needs to be stored. The resulting

moves can be interpreted as MH (or involutive MCMC) moves on an extended state space that includes additional auxiliary random variables $\mathbf{O}_{1:M}^{(1)}, \dots, \mathbf{O}_{1:M}^{(R)}$. The moves are stationary with respect to the following target distribution on the extended state space:

$$p(G, \boldsymbol{\theta} | N, \mathbf{c}, \mathbf{Y}) \frac{1}{R} \sum_{i=1}^R p(\mathbf{O}_{1:M}^{(i)} | N, \mathbf{c}, G, \boldsymbol{\theta}, \mathbf{Y}) \prod_{j \neq i} p(\mathbf{O}_{1:M}^{(j)}) \quad (12)$$

of which the marginal on $(G, \boldsymbol{\theta})$ is the original target distribution $p(G, \boldsymbol{\theta} | N, \mathbf{c}, \mathbf{Y})$.

O Involutive MCMC kernel on scene graph structure and parameters

This section gives details of the involutive MCMC kernel on scene graphs introduced in Section 5.

O.1 Notation for coordinate projections

In several places below, we define sets of tuples using set-builder notation such as

$$X := \{(x, y, z) \mid \text{some condition on } x, y, z\}.$$

In such a case, we may also define coordinate projections that get their names from the formal variables (“ x ,” “ y ,” “ z ”) used in the set-builder expression. Our convention is to denote these coordinate projections by the name proj_\bullet , where \bullet is either a variable name, e.g.,

$$\text{proj}_x(x, y, z) := x$$

or a comma-separated list of variable names, e.g.,

$$\text{proj}_{y,z}(x, y, z) := (y, z).$$

This definition depends not just on the set X , but on the notation used to define it; thus, in the exposition below, we explicitly declare each time we define a function proj_\bullet using the above convention. Note that the name proj_x is to be taken as a single unit, i.e., x does not have independent meaning; in particular, if there is also a variable x in the scope of discourse, the name proj_x does not have anything to do with that variable’s value.

O.2 The number of scene graph structures on a fixed set of objects

Proposition O.2.1. *For a given set of N objects, the number of possible scene graph structures is $(N + 1)^{N-1}$. (Here the root node r is not considered an object.)*

Proof. Let V' be a set of N objects, and let $V := V' \cup \{r\}$. For a given *undirected* tree \tilde{G} on vertices V , there is a unique way to assign edge directions to \tilde{G} to turn it into a directed tree rooted at r . This gives a one-to-one correspondence

$$\text{directed trees on } V \text{ rooted at } r \quad \longleftrightarrow \quad \text{undirected trees on } V.$$

By Cayley [8], the number of undirected trees on V is $(N + 1)^{N-1}$. □

O.3 An involutive MCMC kernel on scene graph structure only

For some set V of vertices and a root vertex $r \in V$, let $\mathbf{G}(V)$ denote the set of directed trees over vertices V rooted at r . For each $G = (V, E) \in \mathbf{G}(V)$ and each $v \in V \setminus \{r\}$, let $S(G, v) \subset V$ denote the vertices of the subtree rooted at v , i.e., the set containing v and its descendants. Let

$$T(G) := \{(v, u) \subset V \times V : v \neq r, u \notin S(G, v)\}. \quad (13)$$

That is, $T(G)$ contains a every pair of vertices (v, u) such that v is not the root note, and u is not a descendant of v . (Intuitively, we can think of $T(G)$ as the set of pairs of vertices (v, u) such that it is possible to sever the subtree rooted at v and re-attach that subtree as a child of u .) Next, let

$$U(V) := \{(G, v, u) : G \in \mathbf{G}(V), (v, u) \in T(G)\} \quad (14)$$

and equip $U(V)$ with coordinate projections $\text{proj}_G, \text{proj}_v$, etc. as in Section O.1. (Intuitively, we can think of the triples $(G, v, u) \in U(V)$ as denoting a graph G , a choice of vertex v at which to sever, and a choice of vertex u at which to graft.) Finally, define the function

$$g : U(V) \rightarrow U(V)$$

by $g(G, v, u) = (G', v, u')$, where (i) u' is the parent of v in G , and (ii) G' is the graph obtained from G by removing the edge (u', v) and adding the edge (u, v) . (By Lemma O.7.1, G' is a tree, so $(G', v, u') \in U(V)$.)

Proposition O.3.1. *The function $g : U(V) \rightarrow U(V)$ is an involution.*

Proof. Let $(G', v', u') := g(G, v, u)$; let $(G'', v'', u'') := g(G', v', u')$; and let E, E' and E'' be the edge sets of G, G' and G'' respectively. Then, by the definition of g , we have $v'' = v' = v$. Also, because G' is a tree that contains the edge (u, v) , it follows that u is the parent of v in G' . Thus $u'' = u$, since u'' is also (by definition) the parent of v in G' . Next, by the definition of g , we have $E' = (E \setminus \{(u', v)\}) \cup \{(u, v)\}$ and

$$E'' = (E' \setminus \{(u, v)\}) \cup \{(u, v)\} = (E \setminus \{(u', v)\}) \cup \{(u', v)\} = E$$

(here we are using the fact that $(u', v) \in E$, which holds by the definition of g). Thus $G'' = G$, so $g(g(G, v, u)) = (G, v, u)$. \square

Proposition O.3.2. *Let $G, G' \in \mathbf{G}(V)$. Then there exists a sequence of triples*

$$(G_0, v_0, u_0), \dots, (G_k, v_k, u_k)$$

satisfying all of the following:

- (i) $(G_i, v_i, u_i) \in U(V)$ for all⁵ $i = 0, \dots, k - 1$
- (ii) $G_0 = G$
- (iii) $G_k = G'$
- (iv) for each $i < k$ we have $G_{i+1} = \text{proj}_G(g(G_i, v_i, u_i))$.

Proof. Let G° denote the scene structure that has no relations between objects; that is,

$$G^\circ := (V, \{(r, v) : v \in V \setminus \{r\}\}).$$

We first prove the result in the case where $G = G^\circ$; then we extend to the general case.

For the case where $G = G^\circ$, the intuition is to work backwards from G' to G° by grafting subtrees onto r until there are no non-singleton subtrees left. Let $G' = (V, E')$, and let $\tilde{E} := \{(u, v) \in E : v \neq r\}$. We then take⁶ $k := |\tilde{E}| - 1$. We define v_i (from the proposition statement) and u'_i (a variable we're now introducing) by arbitrarily choosing an ordered enumeration of \tilde{E} and defining the sequence of pairs $(u'_0, v_0), \dots, (u'_k, v_k)$ to equal that enumeration. Thus,

$$\tilde{E} = \{(u'_0, v_0), \dots, (u'_k, v_k)\}.$$

Next, we define G_i and u_i simultaneously by backward recursion: we take $G_k := G'$ (and choose u_k arbitrarily; the proposition doesn't actually say anything about u_k); and for $0 \leq i < k$, we define G_i and u_i by the equation

$$g(G_{i+1}, v_i, r) = (G_i, v_i, u_i). \quad (15)$$

(To justify the left-hand side being well-defined, we must show $(G_{i+1}, v_i, r) \in U(V)$ for all i . By construction, $v_i \neq r$ for all i , so $r \notin S(G_{i+1}, v_i)$; hence $(G_{i+1}, v_i, r) \in U(V)$.) By applying g to both sides of (15), we get (iv). Finally, note that by induction, G_i has exactly i edges whose source node is not r . Thus $G_0 = G^\circ$. This completes the proof of the case where $G = G^\circ$.

We now move to the general case, where $G \in \mathbf{G}(V)$ is arbitrary. Using the above special case, let $(G_0 = G^\circ, v_0, u_0), (G_1, v_1, u_1), \dots, (G_k, v_k, u_k)$ be a sequence satisfying (i)–(iv) and (15) with $G_0 = G^\circ$. Let $(\bar{G}_0, \bar{v}_0, \bar{u}_0), (\bar{G}_1, \bar{v}_1, \bar{u}_1), \dots, (\bar{G}_k, \bar{v}_k, \bar{u}_k)$ be a sequence satisfying (i)–(iv) and (15)

⁵This proposition doesn't say anything about u_k and v_k ; we leave them in just to simplify the exposition and notation.

⁶Except in the degenerate case where \tilde{E} is empty. In that case we have $G' = G^\circ$, so we simply take $k := 0$, $G_0 := G^\circ$, and u_0 and v_0 to be any vertices.

but with $\bar{G}_0 = G^\circ$ and $\bar{G}_{\bar{k}} = G$. Let $\underline{G}_j := \bar{G}_{\bar{k}-j}$ for $0 \leq j < \bar{k}$ and $\underline{G}_{\bar{k}} := G^\circ$. Substituting $j := \bar{k} - (i + 1)$ into (15) gives

$$g\left(\underline{G}_j, \bar{v}_{\bar{k}-j-1}, r\right) = \left(\underline{G}_{j+1}, \bar{v}_{\bar{k}-j-1}, \bar{u}_{\bar{k}-j-1}\right)$$

for each $j = 0, \dots, \bar{k} - 1$. Thus, letting $\underline{k} := \bar{k}$ and $\underline{v}_j := \bar{v}_{\bar{k}-j-1}$ and $\underline{u}_j := r$, the sequence

$$(\underline{G}_0, \underline{v}_0, \underline{u}_0), \dots, (\underline{G}_{\underline{k}}, \underline{u}_{\underline{k}}, \underline{v}_{\underline{k}})$$

satisfies (i)–(iv) but with $\underline{G}_0 = G$ and $\underline{G}_{\underline{k}} = G^\circ$. Then, the sequence

$$(\underline{G}_0, \underline{v}_0, \underline{u}_0), \dots, (\underline{G}_{\underline{k}-1}, \underline{u}_{\underline{k}-1}, \underline{v}_{\underline{k}-1}), (\underline{G}_{\underline{k}} = G_0 = G^\circ, v_0, u_0), (G_1, v_1, u_1), \dots, (G_k, v_k, u_k)$$

satisfies (i)–(iv): the only piece of this claim that wasn't already proved above is (iv) at the concatenation boundary where G° appears; i.e., it remains only to check that

$$G^\circ = \text{proj}_G(g(\underline{G}_{\underline{k}-1}, \underline{v}_{\underline{k}-1}, \underline{u}_{\underline{k}-1})).$$

Unpacking the definitions, this condition is

$$G^\circ = \text{proj}_G(g(\bar{G}_1, \bar{v}_0, r)),$$

and indeed the condition is satisfied, by (15). \square

For some fixed V with $r \in V$ and $N := |V| - 1$, suppose we have in hand (i) a prior probability distribution $p(G)$ on $G \in \mathbf{G}(V)$; (ii) some data \mathcal{D} ; and (iii) a likelihood function $p(\mathcal{D}|G)$. From these, we can construct an involutive MCMC [12] kernel on the space of graphs $(\mathbf{G}(V))$ by combining the involution g defined above with a family of auxiliary probability distributions $q(v, u; G)$ on $V \times V$ such that $q(v, u; G) > 0$ if and only if $(v, u) \in T(G)$. The kernel takes as input a graph G , samples $(v, u) \sim q(\cdot; G)$, computes $(G', v', u') := g(G, v, u)$, and then returns the new graph G' with probability

$$\min \left\{ 1, \frac{p(G')p(\mathcal{D}|G')q(v', u'; G')}{p(G)p(\mathcal{D}|G)q(v, u; G)} \right\} \quad (16)$$

and otherwise returns the previous graph G (i.e. rejects). Because this kernel satisfies the requirements of involutive MCMC, it is stationary with respect to the following target distribution on $\mathbf{G}(V)$:

$$p(G|\mathcal{D}) = \frac{p(G)p(\mathcal{D}|G)}{\sum_{G' \in \mathbf{G}(V)} p(G')p(\mathcal{D}|G')} \quad (17)$$

Furthermore, if $p(G) > 0$ and $p(\mathcal{D}|G) > 0$ for all $G \in \mathbf{G}(V)$, then the Markov chain generated by repeated application of this kernel converges to the target distribution as the number of steps goes to infinity (the chain is irreducible by Prop. O.3.2 and aperiodic since the proposal has a positive probability of choosing u to be the parent of v , and in that case $G' = G$).

O.4 Transforming between two alternative 6DoF pose parametrizations

Before defining our full involutive MCMC kernel on scene graphs, we define a transformation between continuous parameter spaces that will be used as a building block of the full kernel.

Objects v that are children of the root vertex have their 6DoF pose relative to the world coordinate frame parametrized directly via $\theta_v \in SE(3)$. Recall that the pose of an object v that is child of another object u' is parametrized via the relative pose between a face of u' and a face of v . We choose a parametrization for the pose of one face relative to another that makes it natural to express a prior distribution in which: (i) the two faces are nearly in flush contact with high probability, and (ii) we know little about the relative in-plane offset of the two faces and their relative in-plane orientation. A natural parametrization for this prior uses:

- Two dimensions for the in-plane offset ($a \in \mathbb{R}$ and $b \in \mathbb{R}$) with relatively broad priors
- One dimension for the perpendicular offset ($z \in \mathbb{R}$) with a concentrated prior
- An (outward) face normal vector ($\nu \in S^2$) with a prior that concentrates on anti-parallel face normals

- One dimension of in-plane angular rotation ($\varphi \in S^1$) with a uniform prior.

We now define a bijection

$$\begin{aligned} \xi : \mathbb{R}^3 \times SO(3) &\supseteq \mathbb{R}^3 \times \{\omega \in SO(3) : \omega(0, 0, 1)^\top \neq (0, 0, -1)\} \\ &\rightarrow \mathbb{R} \times \mathbb{R} \times \mathbb{R} \times (S^2 \setminus \{(0, 0, -1)^\top\}) \times S^1 \subseteq \mathbb{R} \times \mathbb{R} \times \mathbb{R} \times S^2 \times S^1. \end{aligned} \quad (18)$$

Note that ξ is a.e. bijective on the supersets as well, in the sense that in (18), ξ is a bijection between the subsets, and each of the subsets has a complement of measure zero in its superset. In ξ , the first three coordinates are copied directly and the orientations are transformed as follows.

In the first parameter space, $SO(3)$, orientations are represented “directly,” as the linear transformation that carries the parent coordinate frame to the child coordinate frame (translated to have the same origin). The base measure on $SO(3)$ is the Haar measure.

In the second parameter space, $S^2 \times S^1$, orientations are represented in Hopf coordinates [44]: intuitively, these coordinates characterize a rotation by where it carries the north pole $(0, 0, 1)^\top$ (we call this $\eta \in S^2$) and how much planar rotation it does after carrying the north pole to η (we call this $\varphi \in S^1$). However, there is no globally consistent (i.e., jointly continuous in η and φ) way to choose where the rotation corresponding to φ “starts” (i.e. which orientations have $\varphi = 0$)—formally, the fiber bundle induced by the Hopf fibration is not a trivial bundle. But, it is possible to make these choices consistently on an open subset of $S^2 \times S^1$ whose complement has measure zero, as we do in Section O.6.2. In particular, provided that η is not the south pole $(0, 0, -1)$, there is a unique unit quaternion $(w, x, y, z) \in S^3$ that satisfies $\text{spin}(w, x, y, z)(0, 0, 1)^\top = \eta$ and has minimal geodesic distance to the identity (where $\text{spin} : S^3 \rightarrow SO(3)$ is the usual covering map, described in Section O.6.1). Then, $\text{spin}(w, x, y, z) \in SO(3)$ is the rotation we take to correspond to $\eta = \eta$, $\varphi = 0$. The resulting map $(S^2 \setminus \{(0, 0, -1)^\top\}) \times S^1 \rightarrow SO(3)$ is smooth; in Section O.6.2 we compute the mapping explicitly in terms of coordinates.

O.5 Full involutive MCMC kernel on scene graphs

Our full involutive MCMC kernel on scene graphs (including their parameters θ) is based on an extension of the involution g defined above. We first define the latent space of pairs (G, θ) , as:

$$X := \bigsqcup_{G \in \mathbf{G}(V)} \left(\left(\prod_{\substack{v \in V \setminus \{r\} \\ (r,v) \in E}} SE(3) \right) \times \left(\prod_{\substack{v \in V \setminus \{r\} \\ (r,v) \notin E}} (F \times F \times \mathbb{R} \times \mathbb{R} \times \mathbb{R} \times S^2 \times S^1) \right) \right) \quad (19)$$

(\sqcup denotes disjoint union), and we endow this set with a reference measure μ_P formed by sums (over the disjoint union) of product measures that are composed from: the Lebesgue measure on \mathbb{R} , the Haar measure on $SO(3)$, the uniform (spherical) measures on S^2 and S^1 , and the counting measure on $F \times F$. Then, we define the space of auxiliary variables as:

$$Y := \{(v, r) : v \in V \setminus \{r\}\} \sqcup \{(v, u, f, f') : v, u \in V \setminus \{r\} \text{ and } f, f' \in F\} \quad (20)$$

with the reference measure μ_Q being the counting measure. We define an auxiliary probability distribution $q(y; G, \theta)$ such that

$$\begin{aligned} q(v, r; G, \theta) &> 0 && \text{for all } v \in V \setminus \{r\} \\ q(v, u, f, f'; G, \theta) &> 0 && \text{for all } (v, u) \in T(G) \text{ and all } f, f' \in F \\ q(y; G, \theta) &= 0 && \text{otherwise.} \end{aligned} \quad (21)$$

The extended state space of the involutive MCMC kernel is then

$$Z := \{(x, y) \in X \times Y : p(x)q(y; x) > 0\}. \quad (22)$$

We construct an involution h on the space Z using the graph involution g defined above as a building block. In particular, Z consists of tuples of four forms, and we define the involution h piecewise depending on which of these four forms the input has: we take

$$Z = Z_1 \sqcup Z_2 \sqcup Z_3 \sqcup Z_4$$

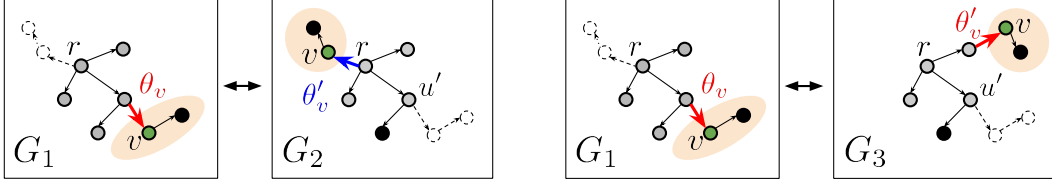


Figure 13: A subset of the possible transition types for our involutive MCMC kernel on scene graphs. Left: ‘contact to floating’ (forwards) and ‘floating to contact’ (backwards). Right: ‘contact to contact’ (forwards) and ‘contact to contact’ (backwards). The vertex v is the chosen ‘sever’ vertex, and its subtree $S(G, v)$ is shaded. Parameters $\theta_v \in SE(3)$, which are the independent 6DoF pose of an object relative to the world coordinate frame, are shown in blue; and parameters $\theta_v \in F \times F \times \mathbb{R} \times \mathbb{R} \times \mathbb{R} \times S^2 \times S^1$, which parametrize the pose of an object relative to another object (specifically the relative pose between two faces of the two objects) are shown in red.

where the definitions of Z_1, Z_2, Z_3, Z_4 , and the parametric form that θ_v takes on each component, are as follows:

$$\begin{aligned}
 Z_1 &:= \{(G, v, r, \theta) : (r, v) \in E\} & \theta_v &\in SE(3) \\
 Z_2 &:= \{(G, v, r, \theta) : (r, v) \notin E\} & \theta_v &\in F \times F \times \mathbb{R} \times \mathbb{R} \times \mathbb{R} \times S^2 \times S^1 \\
 Z_3 &:= \{(G, v, u, \theta, f, f') : u \neq r, (r, v) \in E\} & \theta_v &\in SE(3) \\
 Z_4 &:= \{(G, v, u, \theta, f, f') : u \neq r, (r, v) \notin E\} & \theta_v &\in F \times F \times \mathbb{R} \times \mathbb{R} \times \mathbb{R} \times S^2 \times S^1.
 \end{aligned}$$

We define coordinate projections proj_\bullet on Z_1 and Z_2 (for the free parameters G, v, θ), and on Z_3 and Z_4 (for the free parameters G, u, θ, f, f'), as in Section O.1. Also, for notational convenience below, we extend proj_u to Z_1 and Z_2 by defining $\text{proj}_u(G, v, r, \theta) := r$; i.e., proj_u is constant on $Z_1 \sqcup Z_2$ with value r .

Then, h is defined piecewise as follows:

$$h(z) = \begin{cases} h_{f \rightarrow f}(z) & \text{if } z \in Z_1 \quad (\text{floating to floating}) \\
 h_{c \rightarrow f}(z) & \text{if } z \in Z_2 \quad (\text{contact to floating}) \\
 h_{f \rightarrow c}(z) & \text{if } z \in Z_3 \quad (\text{floating to contact}) \\
 h_{c \rightarrow c}(z) & \text{if } z \in Z_4 \quad (\text{contact to contact}). \end{cases} \quad (23)$$

We next define the function $h_{\bullet \rightarrow \bullet}$ corresponding to each of these four components, and give the acceptance probability in each case (the acceptance probabilities will be derived later in this section).

Floating to floating This transition makes no change to the structure G or the parameters θ :

$$h_{f \rightarrow f}(G, v, r, \theta) := (G, v, r, \theta) \quad (\text{no change}) \quad (24)$$

Contact to floating This transition severs the edge from the parent of v in G (another object) and replaces it with a new edge from the root r to v in G' . The parameters of all vertices other than v are unchanged. The parameters θ_v are set to the absolute pose (relative to r) of v in (G, θ) :

$$h_{c \rightarrow f}(G, v, r, \theta) := (G', v, u', \theta', f, f'),$$

where

$$\begin{aligned}
 (G', v, u') &= g(G, v, r) \\
 (f, f') &= \text{proj}_{f, f'}(\theta_v) \\
 \theta'_w &= \theta_w \text{ for } w \neq v \\
 \theta'_v &= \mathbf{x}_v(G, \theta) \quad (\text{pose of } v \text{ with respect to } r \text{ in } (G, \theta))
 \end{aligned}$$

Floating to contact This transition severs the edge from the parent of v in G (which is r) and replaces it with a new edge from another (object) vertex u to v in G' . The parameters of all vertices other than v are unchanged. The parameters θ_v are computed by (i) computing the relative pose

$\Delta \mathbf{x}_{(u,f') \rightarrow (v,f)}(G, \boldsymbol{\theta}) \in SE(3)$ between the face f of object v (oriented according to its outward normal) and face f' of object u in $(G, \boldsymbol{\theta})$, and then (ii) transforming this pose into an element of $\mathbb{R} \times \mathbb{R} \times \mathbb{R} \times S^2 \times S^1$ via the function ξ defined in Section O.4:

$$h_{f \rightarrow c}(G, v, u, \boldsymbol{\theta}, f, f') := (G', v, r, \boldsymbol{\theta}'),$$

where

$$\begin{aligned} (G', v, r) &= g(G, v, u) \\ \theta'_w &= \theta_w \text{ for } w \neq v \\ \theta'_v &= (f, f', a, b, z, \eta, \varphi) \\ (a, b, z, \eta, \varphi) &= \xi(\Delta \mathbf{x}_{(u,f') \rightarrow (v,f)}(G, \boldsymbol{\theta})) \end{aligned}$$

Contact to contact This transition severs the edge from the parent of v in G (which is some object u') and replaces it with a new edge from another object u to v in G' . The parameters of all vertices other than v are unchanged. The parameters θ_v are again computed by first computing the relative pose computing the relative pose $\Delta \mathbf{x}_{(u,f') \rightarrow (v,f)}(G, \boldsymbol{\theta}) \in SE(3)$, then applying ξ :

$$h_{c \rightarrow c}(G, v, u, \boldsymbol{\theta}, f, f') := (G', v, u', \boldsymbol{\theta}', f_2, f'_2)$$

where

$$\begin{aligned} (G', v, u') &= g(G, v, u) \\ \theta'_w &= \theta_w \text{ for } w \neq v \\ \theta'_v &= (f, f', a, b, z, \eta, \varphi) \\ (f_2, f'_2) &= \text{proj}_{f,f'}(\theta_v) \\ (a, b, z, \eta, \varphi) &= \xi(\Delta \mathbf{x}_{(u,f') \rightarrow (v,f)}(G, \boldsymbol{\theta})) \end{aligned}$$

Proposition O.5.1. *The function h is an involution.*

Proof. First note that in each of the four cases ($z \in Z_i$ for $i = 1, 2, 3, 4$), we have

$$\text{proj}_{G,v,u}(h(z)) = g(\text{proj}_{G,v,u}(z)).$$

Therefore, since g is an involution, we have

$$\text{proj}_{G,v,u}(h(h(z))) = g(\text{proj}_{G,v,u}(h(z))) = g(g(\text{proj}_{G,v,u}(z))) = \text{proj}_{G,v,u}(z).$$

Next, note that if $z \in Z_2 \sqcup Z_4$, then $\text{proj}_{f,f'}(h(h(z))) = \text{proj}_{f,f'}(z)$ simply by unraveling the definitions.

It remains to show that $\text{proj}_{\boldsymbol{\theta}}(h(h(z))) = \text{proj}_{\boldsymbol{\theta}}(z)$. This clearly holds when $z \in Z_1$, as $h_{f \rightarrow f}$ is the identity.

For the case $z \in Z_2$, let $z = (G, v, r, \boldsymbol{\theta})$, and let $f, f' := \text{proj}_{f,f'}(\theta_v)$, and let G and u be such that $g(G, v, r) = (G', v, u')$. Then, unraveling the definitions, we have

$$\text{proj}_{\boldsymbol{\theta}}(h(z)) = \left\{ \begin{array}{l} w \mapsto \theta_w \text{ for } w \neq v \\ v \mapsto \mathbf{x}_v(G, \boldsymbol{\theta}) \end{array} \right\}.$$

Unraveling the definitions one step further, we have

$$\text{proj}_{\boldsymbol{\theta}}(h(h(z))) = \left\{ \begin{array}{l} w \mapsto \theta_w \text{ for } w \neq v \\ v \mapsto (f, f', \xi \left(\underbrace{\Delta \mathbf{x}_{(u',f') \rightarrow (v,f)} \left(G', \left\{ \begin{array}{l} w \mapsto \theta_w \text{ for } w \neq v \\ v \mapsto \mathbf{x}_v(G, \boldsymbol{\theta}) \end{array} \right\} \right)}_{:= \theta''_v := (a', b', z', \eta', \varphi')} \right) \end{array} \right\}.$$

So we need to show $\theta''_v = \theta_v$. By construction, θ''_v is the contact-parametrized relative pose for v (face f) relative to u' (the parent of v in G , face f') that, when converted to an absolute (relative to r) pose in the scene graph $(G, \boldsymbol{\theta})$, gives $\mathbf{x}_v(G, \boldsymbol{\theta})$. In other words, indeed $\theta''_v = \theta_v$.

For the case $z \in Z_3$, let $z = (G, v, u, \theta, f, f')$ and $G' := \text{proj}_G(g(G, v, u))$. Unraveling two layers of definitions similarly to above, we have

$$\text{proj}_\theta(h(h(z))) = \left\{ \begin{array}{l} w \mapsto \theta_w \quad \text{for } w \neq v \\ v \mapsto \mathbf{x}_v \left(\underbrace{G', \left\{ \begin{array}{l} w \mapsto \theta_w \quad \text{for } w \neq v \\ v \mapsto \Delta \mathbf{x}_{(u,f) \rightarrow (v,f')}(G, \theta) \end{array} \right\}}_{:= \theta'_v} \right) \end{array} \right\}.$$

It again suffices to show $\theta'_v = \theta_v$. By construction, θ'_v is the pose in world frame (relative to r) of object v in G' ; and the contact-parametrized relative pose of v (face f) relative to u (face f') in G' by construction has the property that, when converted to an absolute pose in (G, θ) , the result is θ_v . Thus $\theta'_v = \theta_v$.

For the case $z \in Z_4$, let $z = (G, v, u, \theta, f, f')$, and let $(f_2, f'_2) := \text{proj}_{f,f'}(\theta_v)$, and let G' and u' be such that $(G', v, u') = g(G, v, u)$. Unraveling two layers of definitions again, we have

$$\text{proj}_\theta(h(h(z))) = \left\{ \begin{array}{l} w \mapsto \theta_w \quad \text{for } w \neq v \\ v \mapsto (f, f', \xi \left(\underbrace{\Delta \mathbf{x}_{(u',f'_2) \rightarrow (v,f_2)} \left(G', \left\{ \begin{array}{l} w \mapsto \theta_w \quad \text{for } w \neq v \\ v \mapsto (f, f', \xi (\Delta \mathbf{x}_{(u,f') \rightarrow (v,f)}(G, \theta)), f, f' \right) \right\}}_{:= \theta'_v := (a', b', z', \eta', \varphi')} \right) \right) \end{array} \right\}.$$

It again suffices to show $\theta'_v = \theta_v$. Similarly to the above, θ'_v is a contact-parametrized relative pose for v (face f) relative to u' (the parent of v in G , face f') defined by the property that it produces the same absolute pose for v as a second contact-parametrized relative pose. This second relative pose is for v (face f_2) relative to u' (face f'_2) that by construction produces the same absolute pose as v has in (G, θ) . It again follows that $\theta'_v = \theta_v$, and this completes the proof. \square

The automated involutive MCMC implementation in Gen [13] includes an optional dynamic check that applies the involution twice to check that it is indeed an involution. We applied this check during testing of the algorithm to gain confidence in our implementation.

0.6 The Radon–Nikodym derivative

The acceptance ratio for involutive MCMC [12] includes a “generalized Jacobian correction” term, equal to the Radon–Nikodym derivative of a pushforward measure μ_* with respect to a base measure μ defined on the state space Z (μ is constructed the product measure of μ_P and μ_Q [12]). Next, $\mu_* := \mu \circ h^{-1}$ is the pushforward of μ by the involution $h : Z \rightarrow Z$ described above. To justify the validity of this involutive MCMC kernel, we must show that μ_* is absolutely continuous with respect to μ , i.e., that the Radon–Nikodym derivative $\frac{d\mu_*}{d\mu}$ exists. Because all the discrete choices in the model (graph structure, contact faces, etc.) are assigned positive probability mass in both the model and the proposal, it suffices to show absolute continuity for the continuous part of the involution: the mapping (call it ℓ°) that, for given contact faces $f, f' \in F$, converts between a 6DoF pose $\theta_1 \in SE(3)$ and a contact-parameterized relative pose $\theta_2 = (a, b, z, \eta, \varphi) \in \mathbb{R} \times \mathbb{R} \times \mathbb{R} \times S^2 \times S^1$ (note that in this section we use θ_2 to denote only the continuous part of the contact-parameterized relative pose).

Note that ℓ° depends on not just θ_1 , but also on the scene graph, objects and faces $(G, \theta, v, u', f, f')$. Specifically, the absolute pose θ_1 is gotten by pre- and post-composing $\Delta \mathbf{x}_{(u',f') \rightarrow (v,f)}(G, \theta)$ with rigid motions that depend on the absolute poses of face f' of u and face f of v in scene graph (G, θ) , but these rigid motions do not depend on θ_1 or θ_2 themselves. Thus, in the sections below, rather than ℓ° itself, we analyze ℓ , the variant of ℓ° which operates on 6DoF relative poses $\Delta \mathbf{x}$ where ℓ° operates on 6DoF absolute poses \mathbf{x} . Because rigid transformations are diffeomorphisms and their Radon–Nikodym derivatives (Jacobian determinants) are identically 1, the results in the sections below, which show that ℓ has a Radon–Nikodym derivative that is piecewise constant on $A \sqcup B$ (defined below), apply equally well to the map ℓ° which parameterizes θ_1 relative to the world coordinate frame in some particular scene graph.

We can denote a rigid motion by the pair (\mathbf{t}, ω) , where $\mathbf{t} \in \mathbb{R}^3$ is the translation component and $\omega \in SO(3)$ is the rotation component. (In algebraic terms, we are identifying SE_3 with the semidirect

product $\mathbb{R}^3 \times SO(3)$.) Accordingly, define projection functions $\text{proj}_{\mathbf{t}}$ and proj_{ω} on $SE(3)$ as in Section O.1.

Let $Z := A \sqcup B$ where $A := \mathbb{R}^3 \times SO(3)$ and $B := \mathbb{R} \times \mathbb{R} \times \mathbb{R} \times S^2 \times S^1$, and let ν denote the base measure on Z .⁷ In the sections below, we discuss the pushforward $\nu_* := \nu \circ \ell^{-1}$ and its Radon–Nikodym derivative $\frac{d\nu_*}{d\nu}$.

O.6.1 Existence of the Radon–Nikodym derivative

In this section, we prove $\nu_* \ll \nu$. Because $\nu_* = \nu \circ \ell^{-1}$, the proof proceeds by analyzing the involution ℓ . First we show that ℓ is defined almost everywhere, so that ν_* is well-defined. Then we show that there exists a subset $Z'' \subseteq Z$ whose complement has measure zero, such that the restriction of ℓ to Z'' is a diffeomorphism. It follows that $\nu_* \ll \nu$ by [29, Prop 6.5], since ℓ^{-1} is a smooth map.

First, to show that ν_* is well-defined, we show that ℓ is defined almost everywhere on Z . Indeed, the domain of ℓ is $A' \sqcup B'$, where $A' := \mathbb{R}^3 \times \text{domain}(\xi)$ and $B' := \mathbb{R} \times \mathbb{R} \times \mathbb{R} \times \text{domain}(\xi^{-1})$ (where ξ is as defined in Section O.4). Now, $\text{domain}(\xi) = \{\omega \in SO(3) : \omega(0, 0, 1)^\top \neq (0, 0, -1)^\top\}$ has a complement of measure zero in $SO(3)$, and $\text{domain}(\xi^{-1}) = (S^2 \setminus \{(0, 0, -1)^\top\}) \times S^1$ has a complement of measure zero in $S^2 \times S^1$, so indeed $\text{domain}(\ell) = A' \sqcup B'$ has a complement of measure zero in Z .

Next, we show that there exist subsets $A'' \subseteq A'$, $B'' \subseteq B'$, whose complements also have measure zero, such that ℓ fixes $A \sqcup B$ setwise and the restriction of ℓ to $A'' \sqcup B''$ is a diffeomorphism. First, note that the coordinates \mathbf{t} in A and the coordinates a, b, z in B represent the same translation in a different coordinate frame. Thus, for any fixed $\omega \in SO(3)$, the function $\mathbf{t} \mapsto \text{proj}_{a,b,z}(\ell(\mathbf{t}, \omega))$ is a rigid motion, hence a diffeomorphism. Furthermore, the rotation component of $\ell(\theta)$ (regardless of whether $\theta \in A$ or $\theta \in B$) depends only on the rotation component of θ , not at all on the translation component. Thus, ℓ is a diffeomorphism from A'' to B'' if and only if ℓ^* is a diffeomorphism from $\text{proj}_{\omega}(A'')$ to $\text{proj}_{\eta,\varphi}(B'')$, where $\ell^*(\omega) := \text{proj}_{\eta,\varphi}(\ell(0, \omega))$. Taking $A'' := \mathbb{R}^3 \times A^*$ and $B'' := \mathbb{R} \times \mathbb{R} \times \mathbb{R} \times B^*$, we see that it suffices to find subsets $A^* \subseteq SO(3)$ and $B^* \subseteq S^2 \times S^1$ whose complements have measure zero, such that the restriction of ℓ^* to A^* is a diffeomorphism onto B^* .

Denote elements of $SO(3)$ as $\omega = \text{spin}(w, x, y, z)$, where $\text{spin} : S^3 \rightarrow SO(3)$ is the 2-to-1 smooth covering map that carries a unit quaternion $w + x\mathbf{i} + y\mathbf{j} + z\mathbf{k}$ to its corresponding rotation. Then, we take

$$\begin{aligned} A^* &= \{\text{spin}(w, x, y, z) \mid (w, x, y, z) \in S^3; z \neq 0\} \\ B^* &= \{((a, b, c), \varphi) \in S^2 \times S^1 \mid c \neq \pm 1\} \end{aligned}$$

To show that ℓ is a diffeomorphism from A^* to B^* , we give an explicit formula for ℓ^* in terms of coordinates below (Section O.6.2).

O.6.2 Formula for the mapping in coordinates

In this section we give an explicit formula for the map ℓ^* defined in Section O.6.1 in terms of coordinates. For elements $\omega = \text{spin}(w, x, y, z) \in A^*$, the S^2 component of $\ell^*(\omega)$ is the image of $(0, 0, 1)^\top$ under the rotation, and is given by [20, §8.2]:

$$\eta = \text{spin}(w, x, y, z) \begin{pmatrix} 0 \\ 0 \\ 1 \end{pmatrix} = \begin{pmatrix} 2(xz + wy) \\ 2(yz - wx) \\ 1 - 2(x^2 + y^2) \end{pmatrix}.$$

Even though (w, x, y, z) is not uniquely determined by $\text{spin}(w, x, y, z)$, the above expression is well-defined because both possible choices of quaternion— (w, x, y, z) and $(-w, -x, -y, -z)$ —give the same value for the right-hand side.

To compute the S^1 component φ , note that the set of all rotations that carry $(0, 0, 1)^\top$ to η is

$$\{\text{spin}(w, x, y, z) \circ R_{(0,0,1)}(-\varphi') : 0 \leq \varphi' < 2\pi\},$$

⁷That is, the sum of (i) the product of Lebesgue measure on \mathbb{R}^3 and Haar measure on $SO(3)$, and (ii) the product of Lebesgue measure on $\mathbb{R} \times \mathbb{R} \times \mathbb{R}$, spherical uniform measure on S^2 , and uniform spherical measure on S^1 .

where $R_{(0,0,1)}(\varphi')$ is a rotation about the axis $(0, 0, 1)^\top$ by angle φ' . Because the action of S^3 on itself by quaternion multiplication is a geometric rotation of S^3 (in particular, an isometry) [20, §8.3], minimizing geodesic distance among the above family of rotations is equivalent to minimizing (over φ') geodesic distance from $R_{(0,0,1)}(\varphi')$ to (w, x, y, z) . Explicitly, $R_{(0,0,1)}(\varphi')$ corresponds to the unit quaternions

$$\pm (\cos(\varphi'/2), 0, 0, \sin(\varphi'/2)).$$

Note that minimizing geodesic distance on the sphere S^3 is equivalent to minimizing the cosine between the corresponding vectors in $S^3 \subseteq \mathbb{R}^4$. By the cosine double angle formula, the cosine between $R_{(0,0,1)}(\varphi')$ and (w, x, y, z) in this sense is

$$2 \left(\pm (\cos(\varphi'/2), 0, 0, \sin(\varphi'/2)) \cdot (w, x, y, z) \right)^2 - 1,$$

where \cdot denotes the dot product in \mathbb{R}^4 . This quantity is maximized precisely when the dot product is either maximized or minimized, so we can drop the \pm . We can then compute the minima and maxima of the dot product by setting the derivative equal to zero: we have

$$(\cos(\varphi'/2), 0, 0, \sin(\varphi'/2)) \cdot (w, x, y, z) = w \cos(\varphi'/2) + z \sin(\varphi'/2)$$

and the above expression is minimized or maximized when

$$\varphi'/2 = \arctan(z/w) + \pi n \quad \text{for some } n \in \mathbb{Z}$$

or equivalently, $\varphi' = 2 \arctan(z/w) + 2\pi n$. Thus, the S^1 component of $\ell^*(\text{spin}(w, x, y, z))$ that we set out to compute is

$$\varphi = 2 \arctan(z/w),$$

where the branch cut in \arctan is chosen so that the output lies in the interval $[0, \pi)$, and we allow z/w to lie on the extended real line, with $\arctan(\pm\infty) = \pi/2$.

Since $z \neq 0$ in A^* , φ never lands on the branch cut. Thus, $\ell^*(\text{spin}(w, x, y, z))$ is a smooth function of the quaternion (w, x, y, z) . Because spin is a smooth covering map [29, ch. 4], it follows⁸ that spin is also a smooth function of the element $\omega = \text{spin}(w, x, y, z) \in SO(3)$.

The above definition expresses in coordinates the geometry of Hopf fibration and choice of branch cut described in Section O.4. We now need only show that ℓ^* has a smooth inverse. For elements $(\eta, \varphi) \in B^*$, we take [4, §7]

$$\begin{aligned} (\ell^*)^{-1}((a, b, c), \varphi) = \\ \text{spin} \left(\frac{1}{\sqrt{2(1+c)}} ((1+c) \cos(\varphi), a \sin(\varphi) - b \cos(\varphi), a \cos(\varphi) + b \sin(\varphi), (1+c) \sin(\varphi)) \right). \end{aligned}$$

This function is clearly smooth on B^* , and direct computation shows that $(\ell^*)^{-1} \circ \ell^*$ is the identity.

O.6.3 Value of the Radon–Nikodym derivative

In the preceding sections we showed that $\nu_* := \nu \circ \ell^{-1}$ has a density with respect to ν , the Radon–Nikodym derivative $\rho := \frac{d\nu_*}{d\nu}$. In this section we argue that ρ is (a.e.) constant on each of the connected components A and B . Because h acts as isometries on the translation components, and acts on rotation components in a way that doesn't depend on the translation components, we need only look at orientation components. That is, the Radon–Nikodym derivative ρ is equal to the Radon–Nikodym derivative of the pushforward ν_*^* of the base measure⁹ ν^* on $A^* \sqcup B^*$ by ℓ^* :

$$\frac{d\nu_*}{d\nu}(\mathbf{t}, \omega) = \frac{d\nu_*^*}{d\nu^*}(\omega) \quad \text{and} \quad \frac{d\nu_*}{d\nu}(a, b, z, \eta, \varphi) = \frac{d\nu_*^*}{d\nu^*}(\eta, \varphi).$$

Note the following chain of equivalences: $\frac{d\nu_*}{d\nu}$ is a.e. constant on $A^* \iff \nu_*^*$ is a scalar multiple of the Haar measure on $A^* \iff \nu_*^*$ is invariant under the action of $SO(3)$ on itself by multiplication.

⁸This can be seen by pre-composing h'' with a lifting to one of the sheets in an evenly covered neighborhood of ω .

⁹In this case, sum of the Haar measure on $A^* \subseteq SO(3)$ and the product of uniform measures on $B^* \subseteq S^2 \times S^1$.

We can see that the latter statement holds by noting three things: First, the Haar measure on $SO(3)$ equals the pushforward by spin of the Haar measure on unit quaternions. Next, the action of S^3 on itself by group multiplication is an action by isometries [20, §8.3]. Finally, by [44], the volume element on S^3 equals the product of the volume elements on S^2 and S^1 (here we are using the fact that the Haar measure on S^3 coincides with the Borel measure when it is viewed as a Riemannian manifold). Thus the action of $SO(3)$ on itself by multiplication, when pushed through $(\ell^*)^{-1}$, becomes an action by local isometries on $S^2 \times S^1$, and is thus invariant under the base measure ν^* (which on B^* is the product of uniform measures). Therefore indeed $\frac{d\nu^*}{d\nu^*}$ is a.e. constant on A^* . Since ℓ^* is an involution and $\ell^*(A^*) = B^*$, it follows that $\frac{d\nu^*}{d\nu^*}$ is a.e. constant on B^* , and the values of the Radon–Nikodym derivative on A^* and B^* are reciprocals of each other.

O.6.4 Acceptance probability

For our choice of scaling constants, if we assign total measures $SO(3) \mapsto \pi^2$, $S^2 \mapsto 4\pi$, and $S^1 \mapsto 2\pi$, then the Radon–Nikodym derivative corrections in the involutive MCMC acceptance probability [12] are: 1 (for ‘floating to floating’ and ‘contact to contact’ moves), $(4\pi \cdot 2\pi)/\pi^2 = 8$ (for a ‘floating to contact’ move), and $\pi^2/(4\pi \cdot 2\pi) = 1/8$ (for a ‘contact to floating’ move). This gives the following acceptance probabilities for each of the four possible proposed moves from (G, θ) to (G', θ') that can be proposed within our kernel:

Floating to floating When $u = r$ and $u' = r$, the state is unchanged, and the move always accepts:

$$\alpha = \min \left\{ 1, \frac{p(\mathbf{Y}|N, \mathbf{c}, G', \theta')}{p(\mathbf{Y}|N, \mathbf{c}, G, \theta)} \right\} = 1 \quad (25)$$

Floating to contact When $u \neq r$ and $u' = r$ (we are severing v from the root and grafting v onto another object), the acceptance probability is:

$$\alpha = \min \left\{ 1, \frac{p(\mathbf{Y}|N, \mathbf{c}, G', \theta')}{p(\mathbf{Y}|N, \mathbf{c}, G, \theta)} \frac{p(\theta'|N, \mathbf{c}, G')}{p(\theta|N, \mathbf{c}, G)} \frac{q(v', u'; G')}{q(v, u, f_1, f'_1; G)} \cdot 8 \right\} \quad (26)$$

where $(f_1, f'_1) = \text{proj}_{f, f'}(\theta'_v)$.

Contact to floating When $u = r$ and $u' \neq r$ (we are severing v from an object and grafting v onto the root), the acceptance probability is:

$$\alpha = \min \left\{ 1, \frac{p(\mathbf{Y}|N, \mathbf{c}, G', \theta')}{p(\mathbf{Y}|N, \mathbf{c}, G, \theta)} \frac{p(\theta'|N, \mathbf{c}, G')}{p(\theta|N, \mathbf{c}, G)} \frac{q(v', u', f_2, f'_2; G')}{q(v, u; G)} \cdot \frac{1}{8} \right\} \quad (27)$$

where $(f_2, f'_2) = \text{proj}_{f, f'}(\theta_v)$.

Contact to contact When $u \neq r$ and $u' \neq r$ (we are severing v from an object and grafting v onto another object), the acceptance probability is:

$$\alpha = \min \left\{ 1, \frac{p(\mathbf{Y}|N, \mathbf{c}, G', \theta')}{p(\mathbf{Y}|N, \mathbf{c}, G, \theta)} \frac{p(\theta'|N, \mathbf{c}, G')}{p(\theta|N, \mathbf{c}, G)} \frac{q(v', u', f_2, f'_2; G')}{q(v, u, f_1, f'_1; G)} \right\} \quad (28)$$

where $(f_1, f'_1) = \text{proj}_{f, f'}(\theta'_v)$ and $(f_2, f'_2) = \text{proj}_{f, f'}(\theta_v)$.

O.7 Lemmas

Lemma O.7.1. *Let $G = (V, E)$ be a directed tree rooted at $r \in V$, and suppose $u, u', v \in V$ are such that the following conditions hold:*

- (i) $u \neq v$
- (ii) u is not a descendant of v
- (iii) $(u', v) \in E$.

Let G' be the directed graph obtained from G by deleting the edge (u', v) and adding the edge (u, v) , that is, $G' = (V, (E \setminus \{(u', v)\}) \cup \{(u, v)\})$. Then G' is a directed tree rooted at r .

Proof. We show that for any vertex w , there is a unique path in G' from r to w .

First, suppose w is not a descendant of v in G' . Then w is not a descendant of v in G , since the set of descendants of v is the same in G and G' . Thus no path from r to w in either G or G' passes through v ; consequently, no path from r to w in either G or G' contains either of the edges $(u'v)$ or (u, v) . Thus, a sequence of vertices $r = x_0, x_1, \dots, x_n = w$ is a path in G' if and only if it is a path in G . Since there is a unique path from r to w in G , it follows that there is a unique path from r to w in G' .

Next, suppose w is a descendant of v in G' (and hence also in G). Because u' is the only in-neighbor of v in G , it follows that u is the only in-neighbor of v in G' . Thus, every path from r to w in G' is the concatenation of a path from r to u with a path from v to w . But since u is not a descendant of v in G (hence neither in G'), there is a unique path from r to u in G' , by the above paragraph. And of course, there is a unique path from v to w in G , hence also in G' since the subtrees rooted at v are the same. Therefore there is a unique path from r to w in G' . \square